nuclear fusion
IAEA

PAPER • OPEN ACCESS

Definition of an EU-DEMO design point robust to epistemic plasma physics uncertainties

To cite this article: M. Coleman *et al* 2025 *Nucl. Fusion* **65** 036039

OPEN ACCESS
IOP Publishing | International Atomic Energy Agency
Nuclear Fusion
Nucl. Fusion **65** (2025) 036039 (23pp)
https://doi.org/10.1088/1741-4326/ada6d9

Definition of an EU-DEMO design point robust to epistemic plasma physics uncertainties

M. Coleman[1,2,*], H. Zohm[1,3], C. Bourdelle[1,4], F. Maviglia[1,5], A.J. Pearce[2], M. Siccinio[1,3], A. Spagnuolo[1,6] and S. Wiesen[1,7]

[1] EUROfusion, Boltzmannstr. 2, Garching 85748, Bavaria, Germany
[2] United Kingdom Atomic Energy Authority, Culham Science Centre, Abingdon OX14 3DB, Oxfordshire, United Kingdom of Great Britain and Northern Ireland
[3] Max Planck Institute for Plasma Physics, Boltzmannstr. 2, Garching 85748, Bavaria, Germany
[4] Alternative and Atomic Energies Agency, Cadarache, St. Paul-Lez-Durance F-13108, Bouches-du-Rhône, France
[5] Associazone EURATOM-ENEA sulla Fusione, C. R. Frascati, Frascati 65-00044, Rome, Italy
[6] Karlsruhe Institute for Technology, Hermann-von-Helmholtz-Platz 1, Eggenstein-Leopoldshafen 76344, Baden-Württemberg, Germany
[7] Dutch Institute for Fundamental Energy Research, De Zaale 20, PO Box 6336, Eindhoven 5600 HH, North Bravant, Netherlands

E-mail: Matti.Coleman@ukaea.uk

Received 24 July 2024, revised 19 November 2024
Accepted for publication 7 January 2025
Published 28 February 2025

Abstract

A novel approach for explicitly and robustly accounting for epistemic uncertainties in plasma confinement in the 0D design of tokamaks is presented, in which the plasma safety factor at the 95th percentile flux surface, q_{95}, is used to apply a design margin on confinement in terms of the H-factor, H. The PROCESS code is used to explore the EU-DEMO design space in terms of aspect ratio, major radius, q_{95}, and net electric power, $P_{el,net}$ using the above approach. A comprehensive account of the input assumptions and underlying models used is given. We formulate a proposal for a new EU-DEMO design point which addresses some key shortcomings of the previous design point (EU-DEMO 2017 (Wenninger and Kembleton 2017 *Technical Report* EFDA_D_2NDSKT (EUROfusion); Siccinio *et al* 2022 *Fusion Eng. Des.* **176** 113047)), in particular by the inclusion of an explicit and quantified design margin for epistemic confinement uncertainties, and a considerable reduction in divertor heat loads during re-attachment. We find that self-consistently including a size-able margin on confinement using

* Author to whom any correspondence should be addressed.

our approach considerably reduces the potential $P_{el,net}$ of a reactor, compared with no margin. However, we argue that by doing so, the engineering design of future tokamak fusion power plants can effectively be insulated from epistemic confinement uncertainties insofar as possible, facilitating the design process.

Keywords: fusion reactor, DEMO, systems code, uncertainties, confinement

Some figures may appear in colour only in the online journal

Nomenclature

Notation

$(x)^*$	Quantity x as $q_{95} \rightarrow q_{95,min}$, see equation (1)
Δx	Margin on quantity x
$\langle x \rangle$	Plasma volume-averaged quantity x
$\langle x \rangle_n$	Plasma density-weighted volume-averaged quantity x
$\overline{x}$	Plasma line-averaged quantity x
x_{ped}	Plasma profile value x at the pedestal
x_{sep}	Plasma profile value x at the separatrix

Symbols

β	Ratio of plasma pressure to magnetic energy density
β_N	Normalised β
β_{fi}	Fast alpha contribution to β
$\beta_{thermal}$	Ratio of thermal plasma pressure to magnetic energy density
$\dot{q}_{div,outer}$	Divertor outer target heat flux
ϵ	Inverse aspect ratio
κ	Plasma elongation
κ_a	Area-averaged plasma elongation
κ_{95}	Plasma elongation at the 95th percentile flux surface
ρ	Normalised plasma radial coordinate
σ_{CS}	Hoop stress in the CS conductor
$\sigma_{TF,case}$	Tresca stress in the TF case
$\sigma_{TF,WP}$	Tresca stress in the TF conductor
$\sigma_{VV,TFCFD}$	Hoop stress in the VV during a TFCFD
$\tau_{E,98(y,2)}$	Plasma energy confinement time according to the IPB98(y,2) scaling law [1]
τ_E	Plasma energy confinement time
τ_{pulse}	Plasma pulse length
τ_{TFCFD}	Discharge time constant of the TF coils during a TFCFD
A	Plasma aspect ratio
a	Plasma minor radius
B_P	Poloidal field
$B_{T,TF}$	Peak toroidal field in the TF coil
B_T	Toroidal field at the plasma major radius
c_{Xe}	Constant xenon impurity concentration across the profile
$E_{TF,stored}$	Total TF coil stored magnetic energy
f_{GW}	Greenwald fraction
f_H	Factor for epistemic confinement uncertainties
f_{ind}	Fraction of inductively-produced plasma current
f_{LH}	Factor for epistemic mode access uncertainties
H	Plasma H-factor
$H_{98(y,2)}$	Plasma H-factor according to the IPB98(y,2) scaling law [1]
H_{rc}	Radiation-corrected plasma H-factor, see [2]
I_p	Plasma current
$j_{CS,crit}$	CS winding pack critical current density
j_{CS}	CS winding pack current density
$j_{TF,crit}$	TF winding pack critical current density
j_{TF}	TF winding pack current density
L_{dpa}	Reactor lifetime displacements per atom in EUROfer
L_{fpy}	Full power years required to reach L_{dpa}
l_i	Normalised plasma internal inductance
L_{Z_i}	Volumetric radiative loss function for ion species i
n_e	Electron density
n_i	Ion density
$n_{cycles,CS}$	Number of reactor cycles in the CS coil
n_{cycles}	Number of reactor cycles
n_{GW}	Greenwald density
P_α	Plasma alpha power
P_{add}	Additional plasma heating power
$P_{charged}$	Plasma charged particle power (excluding alphas)
P_{con}	Conduction-convection loss power
$P_{el,BB,pump}$	BB pumping electrical power
$P_{el,building}$	Electrical power for buildings
$P_{el,cryoplant}$	Cryoplant system electrical power
$P_{el,div,pump}$	Divertor pumping electrical power
$P_{el,HCD}$	H&CD electrical power
$P_{el,net}$	Net electrical power
$P_{el,PF}$	PF system electrical power
$P_{el,TF}$	TF system electrical power
$P_{el,tot}$	Gross electrical power
P_{fus}	Plasma fusion power
P_{LH}	Power crossing the separatrix assumed to be required to enter H-mode
P_{net}	Net power delivered to the plasma
P_{ohmic}	Ohmic heating power in the plasma
$P_{rad,core}$	Plasma core radiation power assumed to contribute to P_{net} and used in the τ_E scaling
P_{rad}	Plasma radiation power
P_{sep}	Plasma charged particle power crossing the separatrix
P_{syn}	Plasma synchrotron radiation power
$P_{tot,thermal}$	Total thermal power in the blankets and divertors
Q	Fusion energy gain factor
q	Plasma safety factor

$q_{95,min}$	Minimum or 'worst-case' plasma safety factor at the 95th percentile flux surface
q_{95}	Plasma safety factor at the 95th percentile flux surface
q_{cyl}	Equivalent cylindrical plasma safety factor at the edge
R_0	Plasma major radius
R_{plasma}	Plasma resistance
S_{plasma}	Plasma surface area
T_e	Electron temperature
T_i	Ion temperature
v_{loop}	Plasma loop voltage
V_{plasma}	Plasma volume
W_{th}	Plasma thermal energy
Z	Ion charge
Z_{eff}	Plasma effective charge

1. Introduction

The last official EU-DEMO 0D baseline was produced in 2017 [3, 4], using PROCESS [5, 6], in anticipation of the G1 Gate Review [7]. This design point, which we refer to here as the EU-DEMO 2017 baseline, was issued to the broader EUROfusion members and was investigated and developed in detail for many years. Despite the best efforts of the team to develop a robust and conservative design, during this period, and at the G1 Gate Review in 2020, several major issues with the design were identified:

(i) the high sensitivity of plasma performance to confinement assumptions—and the lack of associated design margin,
(ii) the lack of margin on the safety factor at the 95th percentile flux surface, q_{95}, which was set to 3.0 (considered to be an operational limit),
(iii) the unacceptably high divertor heat fluxes during off-normal re-attachment events (considered to be unavoidable),
(iv) the relatively high toroidal field on axis requiring large and expensive mechanical structures in the cold mass,
(v) the large number of cycles leading to design-driving fatigue issues in the central solenoid (CS),
(vi) and the lack of a viable solution for breeding blanket (BB) remote maintenance.

The first point above has required a systematic re-think of how we carry out 0D conceptual design for EU-DEMO. Previously, see [3, 8, 9], the performance of the plasma in terms of fusion power, P_{fus}, was taken as a given and no strategy was explicitly used to account for confinement uncertainties. A strategy for the design of a steady-state machine which falls back to pulsed operation in the case of poor plasma performance was elaborated in [10], in which the plasma current, I_p, was used to recover performance, but was not directly incorporated in the 0D conceptual design of a pulsed EU-DEMO. Here we develop on the approach first outlined in [10], and transform it into a design strategy for EU-DEMO. A practical design margin on epistemic confinement uncertainties is introduced, by means of q_{95}, with an associated performance recovery strategy. We include this approach in the PROCESS systems code [5, 6], modifying the design optimisation problem to self-consistently account for the affected constraints.

In addition, prior to the G1 Gate Review, several options were considered for heating and current drive (H&CD) and BB technologies. The PROCESS design point had been created assuming neutral beam injection (NBI) and Helium-cooled pebble bed (HCPB) blankets. At the time, the assumptions for the HCPB and water-cooled Lithium-Lead (WCLL) blankets were such that they were broadly similar in terms of plant net electrical output, $P_{el,net}$. Since the G1 Gate Review, a decision was taken to use electron cyclotron (EC) heating and current drive only [11], and substantial blanket concept design work [12, 13] led to a divergence in performance, with HCPB blankets now performing better in terms of $P_{el,net}$, see e.g. [14].

Finally, we decided to re-assess what the reactor performance should be in terms of $P_{el,net}$, and pulse length, τ_{pulse}, whilst still respecting the EU-DEMO 'stakeholder requirements' for net electricity, $300 \leqslant P_{el,net} \leqslant 500$ MWe and pulse length, $\tau_{pulse} \geqslant 2$ h.

In this paper, we first outline the EU-DEMO design philosophy (section 2), before describing the novel approach taken for treating plasma physics uncertainties in the design (section 3), the EU-DEMO design study we have carried out (section 4), and the results (section 5).

2. Design philosophy

The EU-DEMO mission and scope are presently under discussion in EUROfusion, but for the purposes of this study it remains unchanged [15, 16]:

(i) Demonstrate tritium self-sufficiency
(ii) Produce net electricity
(iii) Operate safely and reliably over a reasonable time-span
(iv) Act as a component test facility, in particular for breeding blankets

It has always been intended for EU-DEMO to be a realistic machine; that is to say, it is the machine with the highest probability of mission success were construction to start tomorrow. It is the fusion reactor design with the lowest technical risk, which does not mean it is 'low-risk'.

This philosophy puts EU-DEMO in stark contrast with many other devices presently proposed, compared with which EU-DEMO appears consistently unattractive as an economic value proposition[8]. The over-arching principles of EU-DEMO are summarised elsewhere [16], but generally imply relying on modest extrapolations from the ITER physics and technology basis, and the use of proven technologies where possible.

[8] On paper, at least, assuming that all reactors work as intended—that is to say ignoring risk in the value proposition.

The intent is to learn as much as possible from the design, licensing, and construction of ITER, from which there is already much to learn.

As is the case with many design problems, the off-normal load cases very often end up driving the design. Whilst the PROCESS systems code [5, 6] is used for EU-DEMO to define a reactor design point during normal operation, many constraints and input values in fact come from considerations of off-normal events (e.g. maximum vertically stable elongation, toroidal field coil fast discharge (TFCFD) load case on the vacuum vessel, etc).

In this work, we apply this philosophy of conservatism to the epistemic uncertainties in plasma confinement.

3. Margin for plasma physics uncertainties

The lack of predictive physics capability in terms of plasma confinement performance has serious design implications. The effects of epistemic confinement uncertainties have been quantified in the past using PROCESS [17, 18], but a strategy for explicitly accounting for these uncertainties in the design has not been put forward.

3.1. Need for a margin

In sophisticated integrated modelling frameworks, such as JINTRAC [19] or ASTRA [20], turbulent transport is computed by reduced, physics-based models such as QuaLiKiz [21, 22] and TGLF [23, 24] with different saturation rules. At present, none of these models includes the complex interplay between energetic alpha particles, magnetohydrodynamics, and turbulence [25]. Nonetheless, we use them for our predictions and obtain results for P_{fus} ranging from 1.6 to 3.0 GW for a typical EU-DEMO-like machine, see table 1, whereas the IPB98(y,2) scaling law [1] gives 2.0 GW [26].

Systems codes, such as the PROCESS code used in this study, generally rely upon scaling laws to estimate plasma confinement. The choice of scaling law, temperature and density profile parameterisation, profile peaking factors, and associated confinement assumptions have profound consequences on the supposed performance of the plasma.

The discrepancy between integrated modelling and the use of scaling laws with assumed profiles is to be expected: fusion power in plasmas dominated by alpha heating is strongly nonlinearly coupled with heat and particle transport. The transport of heat and particles in the plasma effectively determines the plasma temperature and density profiles and the alpha power, which (as the primary heat source in the plasma) affects the transport. Integrated modelling efforts resolve such nonlinearities along the profile, and predict temperature and density profiles and energy content self-consistently (within the context of the supported physics and the modelling assumptions made). As seen in table 1, estimates vary, and ultimately such predicted profiles required validation in burning plasma experiments. For detailed discussion of the present state of integrated modelling efforts, and why fusion power estimates are challenging, please see [31]. Scaling laws, whilst accounting for power degradation, are derived from multi-machine databases of plasma with negligible alpha power, and the profiles assumed in conjunction with a scaling law are derived or inspired from experiments at $Q < 1$ and/or integrated modelling simulations; arguably not a very robust basis for extrapolation to plasmas dominated by alpha heating.

Table 1. P_{fus} as calculated by different transport models for a representative EU-DEMO design point. Small variations in H can lead to large variations in P_{fus}. Data from [26].

	P_{fus} (GW)	W_{th} (GJ)	$H_{98(y,2)}$
QuaLiKiz [21, 22]	3.0	1.45	1.00
TGLF-SAT0 [27]	2.4	1.3	0.99
TGLF-SAT1 [28]	2.0	1.2	0.98
TGLF-SAT1geo [29]	1.7	1.1	0.94
TGLF-SAT2 [30]	1.6	1.05	0.89

Both approaches ultimately suffer from the same flaw: no conclusive proof of validity in reactor-relevant plasmas. The inability to predict burning plasma performance will persist until such reactor-relevant plasmas are operated.

In the following, we assume that the true performance of the plasma in any given operational scenario in a first-of-a-kind fusion reactor can never be truly known until after commissioning, and that scaling laws and turbulent transport simulations can only yield estimates. Yet even if one believes the scaling laws or the turbulent transport simulations, a factor of 2 variation in P_{fus} (see e.g. table 1)—a fundamental parameter in tokamak design—cannot reasonably or cost-effectively be accommodated for in the conceptual design.

For instance, let us say we have a reactor for which we have the low and high estimates of fusion power from table 1 (P_{fus} = 1.6–3.0 GW). From previous EU-DEMO studies (e.g. [3]) we have $P_{el,net}/P_{fus} \approx 0.25$, which we can use as a crude metric to estimate the net electric output for a given fusion power[9]. Assuming that the reactor could otherwise handle this range of fusion power, and using the aforementioned metric to propagate the uncertainty on P_{fus}, such a reactor could in theory produce $P_{el,net} \approx$ 400–750 MWe. Were one inclined to build the reactor such that it could encompass this range in $P_{el,net}$, the blankets, primary heat transfer system, balance of plant, etc of such a machine would have to be designed accordingly. In practice, this would mean propagating a factor ≈2 to a vast number of load cases (neutron flux, thermal loads, static and cyclic stress amplitudes, etc) with wide-reaching implications

[9] The proposed value for $P_{el,net}/P_{fus}$ is roughly valid for EU-DEMO-like designs, where several hundred MWe are desired and several tens of MW of heating and current drive are employed. Once one accounts for energy multiplication, the various parasitic electrical loads required to operate the reactor, and the thermal to electric conversion efficiency, a value of around 0.25 is typical; e.g. EU-DEMO 2017: 0.248 [3].

on design (shielding thicknesses, coolant flow-rates, pump and heat exchanger dimensioning, cooling towers, etc). This is perhaps not infeasible, but it is certainly an impractically large range from an engineering design perspective, and implies significant over-dimensioning for many systems with considerable capital costs and additional complexity for many systems which are technologically challenging.

3.2. Conditions for a practical margin

As such, it is paramount that a reasonable and practical margin on the performance of the plasma is included in the conceptual design phase. By 'reasonable and practical', we define the following conditions:

(i) That the machine geometry need not be modified (the machine has already been built).
(ii) That no 'upgrades' or new systems are required to be installed.
(iii) That the margin parameter for epistemic uncertainties in plasma performance have a high gain on the performance of the plasma (i.e. that small variations have large effects).
(iv) That design ranges related to plasma uncertainties not be required in systems with relatively high capital cost or low technology readiness level.

The last point is to 'insulate' the designers of technologically challenging systems from having to treat significant unknowns over which they exert little or no influence. Large design ranges lead to more complex constellations of load cases, over-dimensioning, and additional 'engineering' margins which have a tendency to accumulate. Ideally, one would avoid subjecting technologically challenging systems to such uncertainty (on top of what they must already contend with). Similarly one would like to avoid over-dimensioning of systems with large capital cost implications (e.g. not have to buy four steam generators when ultimately only two are required).

3.3. q_{95} as a design margin for plasma physics uncertainties

We need to leverage a parameter on which P_{fus} depends strongly, yet that can be varied without altering the reactor's physical layout. Naturally, R_0 and B_T (which would otherwise be good candidates) are ruled out. The plasma current, I_p, on the other hand can be varied relatively easily, and has a particularly strong effect on P_{fus} if one takes into account the Greenwald density limit, such that $\overline{n_e} \propto I_p$. Fusion power has a direct dependence on density via the reaction rate: $P_{fus} \propto \langle n_e \rangle^2$, and an indirect dependence on plasma current and density via the confinement time, for which (depending on the scaling law used) $\tau_E \propto I_p^a \overline{n_e}^b$, where typically $a+b \approx 1.0$ to 1.4. This leads us to $P_{fus} \propto I_p^{2-3}$, see appendix A for a more complete discussion. Thus, small variations in I_p have a large gain on P_{fus}.

However, $I_p \propto \dfrac{a^2 B_T}{R_0 q_{95}}$, making it unsuitable as an independent variable. Instead, our approach is to use the plasma safety factor at the 95th flux percentile, q_{95}, as the parameter in which the epistemic uncertainties related to plasma confinement are encapsulated.

We focus on the scenario in which the plasma confinement is less good than anticipated, which we assume manifests itself solely in a lower P_{fus}.[10] We chose to attempt to preserve P_{fus} at the nominal design value, as it is directly linked to the high-level performance of the reactor ($P_{el,net}$) and because the blankets (technologically challenging) and primary heat transfer system, balance of plant, etc (capital intensive) would strongly benefit from being able to design around a reference fusion power with little or no margins.

We also chose to preserve B_T, such that the toroidal field coils (technologically challenging) need not have to contend with any large-scale margins in terms of target performance.

The idea is as follows:

(i) Design and build a tokamak with q_{95} above what is considered to be the minimum value for the operational scenario, i.e. $q_{95} > q_{95,min}$.
(ii) If the fusion power is lower than anticipated, reduce $q_{95} \rightarrow q_{95,min}$,
(iii) thereby increasing plasma current, I_p,
(iv) and density, n, commensurately, keeping the Greenwald fraction, f_{GW}, and density profile shape constant.
(v) Repeat until the reference P_{fus} is recovered.

With this approach, the machine geometry, toroidal field, and thermal power can be assumed to be at nominal values during design, with no margins associated with plasma physics uncertainties. Clearly, practically all plasma parameters would now have an associated design range, but with the postulate that P_{fus} is recovered, one can determine to zeroth order the design ranges for key plasma integral parameters.

Note that the choice of a single parameter (q_{95}) to encapsulate epistemic confinement uncertainties is driven out of pragmatism; it being far simpler to keep track of the dependencies on a single parameter than to do so for multiple parameters.

3.4. 0D model for $q_{95} \rightarrow q_{95,min}$

It is useful to have a simplified understanding of the implications of reducing the safety factor in a design point, so that considerations of the margins for epistemic uncertainties can be included in systems codes.

[10] The fortuitous case in which the plasma performs better than expected is relatively straight-forward: the thermal power of the machine would be capped at the nominal value, with almost all systems operating at their nominal load or a less-challenging load case.

In the following, we use the notation $(x)^*$ to denote the value of x as q_{95} is reduced to $q_{95,min}$, see equation (1)

$$(x)^* \equiv \lim_{q_{95} \to q_{95,min}} x. \tag{1}$$

Note that in the postulated scenario described in the previous section, we have:

$$\begin{aligned}
(q_{95})^* &= q_{95,min} \\
(P_{fus})^* &= P_{fus} \\
(B_T)^* &= B_T \\
(R_0)^* &= R_0 \\
(A)^* &= A \\
(\kappa_{95})^* &= \kappa_{95} \\
(\delta_{95})^* &= \delta_{95}.
\end{aligned} \tag{2}$$

The plasma current, I_p, and line-averaged electron density, $\overline{n_e}$, are given by:

$$\begin{aligned}
I_p &= \mathcal{S}\,(A, \kappa_{95}, \delta_{95})\,\frac{a^2 B_T}{R_0 q_{95}} \\
\overline{n_e} &= f_{GW}\frac{I_p}{\pi a^2}
\end{aligned} \tag{3}$$

where $\mathcal{S}$ is a function of the plasma poloidal cross-section, usually taken from a scaling or fit to experimental data, and a is the plasma minor radius ($a \equiv R_0/A$). Taking the equalities from equation (2), we have:

$$(I_p)^* = \frac{q_{95}}{(q_{95})^*} I_p. \tag{4}$$

And at fixed Greenwald fraction:

$$(\overline{n_e})^* = \frac{q_{95}}{(q_{95})^*}\overline{n_e}. \tag{5}$$

To zeroth order, with $(P_{fus})^* = P_{fus}$, ignoring changes in Ohmic heating power, Bremsstrahlung, synchrotron radiation, and core radiation terms, and assuming we remain in H-mode[11], we can state that the conduction-convection power, P_{con}, the 'net' power delivered to the plasma, P_{net}, and the power crossing the separatrix, P_{sep}, are also invariant:

$$\begin{aligned}
(P_{con})^* &= P_{con} \\
(P_{net})^* &= P_{net} \\
(P_{sep})^* &= P_{sep}.
\end{aligned} \tag{6}$$

[11] This is reasonable, as we expect that we can recover the fusion power with relatively modest increases in density. However, it is possible that H-mode can no longer be accessed at higher density. This is discussed in section 4.2.3.

3.5. Correspondance with H

Whilst we have chosen q_{95} here as the parameter with which we account for plasma physics uncertainties, it is of interest to relate this a term which explicitly performs a similar role: the H-factor, H.

From equation (6), we have at thermal equilibrium ($P_{net} = P_{con}$):

$$(P_{net})^* = P_{net} = \frac{W_{th}}{\tau_E} = \frac{(W_{th})^*}{(\tau_E)^*}. \tag{7}$$

As $(P_{fus})^* = P_{fus}$, we have $(W_{th})^* = W_{th}$ and $(\tau_E)^* = \tau_E$.

The confinement time, τ_E, is calculated in PROCESS using a scaling law. In EU-DEMO studies, we use the ITER Physics Basis scaling law IPB98(y,2) [1]:

$$\tau_{E,98(y,2)} = 5.62 \times 10^{-2} \frac{I_p^{0.93} B_T^{0.15} \overline{n}_{e,20}^{0.41} R_0^{1.97} \kappa_a^{0.78} M^{0.19}}{P_{net}^{0.69} A^{0.58}} \tag{8}$$

with $H \equiv \tau_E/\tau_{E,98(y,2)}$, and κ_a the area-averaged elongation.

If we now declare (arbitrarily) the lower-than-anticipated fusion power is due solely to poor confinement quality (i.e. low H), we can derive an expression for $(H)^*$, which is essentially the worst-case confinement quality we can compensate for with $q_{95} \to q_{95,min}$. Splitting out the plasma current and density terms in equation (8), and rearranging equation (7), we have:

$$(H)^* = \left(\frac{I_p}{(I_p)^*}\right)^{0.93} \left(\frac{\overline{n_e}}{(\overline{n_e})^*}\right)^{0.41} H = \left(\frac{(q_{95})^*}{q_{95}}\right)^{1.34} H. \tag{9}$$

We can then define the factor for epistemic confinement uncertainties, f_H, and the associated margin ΔH as:

$$f_H \equiv \frac{H}{(H)^*} \equiv \frac{H}{(1-\Delta H)\,H}. \tag{10}$$

For instance, if one were to take (again, arbitrarily) the root-mean-squared-error of the IPB98(y,2) scaling (14.5 % [1]) as ΔH, this would give:

$$f_H = \frac{H}{(1-0.145)\,H} \iff \left(\frac{q_{95}}{(q_{95})^*}\right)^{1.34} = 1.170 \tag{11}$$

corresponding to a ratio $\dfrac{q_{95}}{(q_{95})^*} = 1.124$, or a necessary design margin on q_{95} of 11.0%.

4. EU-DEMO design study

For any given PROCESS design study, dozens of different assumptions must be made and a variety of models must be selected. Each of these assumptions and models also have a range of associated input parameters. In the interests

Table 2. Summary of the general, fixed input parameters used in this study.

Parameter	Description	Value
ρ_{ped}	Plasma T- and n-profile normalised pedestal radius	0.94
α_T	T-profile exponent	1.45
β_T	T-profile exponent	2.0
α_n	n-profile exponent	1.0
β_n	n-profile exponent	2.0
$f_{GW,ped}$	Imposed fraction of n_{GW} at the pedestal	0.85
$f_{GW,sep}$	Imposed fraction of n_{GW} at the separatrix	0.5
$T_{e,sep}$ (keV)	Electron temperature at the separatrix	0.1
θ_i	Constant ratio of ion to electron temperature	1.0
q_0	Core safety factor	1.0
f_{P_α}	Fraction of alpha power trapped in the plasma	0.95
H_{rc}	Imposed radiation-corrected H-factor	1.1
$r_{\tau,He}$	Imposed ratio of helium to energy confinement time	5.0
ρ_{core}	Normalised radius within which radiation effects are accounted for in τ_E	0.75
$f_{rad,core}$	Fraction of core radiation	0.6
c_W	Constant tungsten concentration across the profile	5×10^{-5}
f_κ	Imposed ratio of κ/κ_{95}	1.12
δ	Plasma edge triangularity	0.5
δ_{95}	Plasma triangularity at the 95th percentile flux surface	0.333
m_s	Stability margin used for calculating maximum vertically stable elongation	0.2
e_{mult}	Energy multiplication factor	1.2
$\eta_{thermal}$	Thermal to electric conversion efficiency	0.316
f_{syn}	Synchrotron wall reflection coefficient	0.6
C_{Ejima}	Ejima coefficient for resistive poloidal flux consumption during ramp-up	0.2
P_{CD} (MW)	EC current drive power	40
P_{heat} (MW)	EC heating power	10
γ_{ECCD} (10^{20}A W^{-1} m^{-2})	Normalised electron cyclotron current drive efficiency	0.3
η_{EC}	Electron cyclotron wall-plug efficiency	0.4
$\eta_{pump,isen}$	BB pump isentropic efficiency	0.85
$\eta_{pump,electrical}$	BB pump electrical efficiency	0.9
L_{dpa} (dpa)	Lifetime of the reactor in displacements per atom at the outboard midplane in EUROfer	70

of transparency and reproduce-ability, we attempt to give a complete description of the assumptions, models, and input parameters used in this study, see the next sub-section.

In section 4.2, we discuss the various constraints and bounds applied to the design optimisation problem, described in section 4.4.

4.1. Assumptions and inputs

The input parameters fixed for this design study are summarised in tables 2–4, and discussed in more detail throughout this sub-section.

4.1.1. Plasma profiles and confinement assumptions.

PROCESS has a simplified representation of the plasma, with simple parabolic-with-pedestal profile representations of T and n, shown in equation (12) for an arbitrary quantity X, [5].

$$X(\rho) = \begin{cases} X_{ped} + \left(X_{core} - X_{ped}\right)\left(1 - \left(\dfrac{\rho}{\rho_{ped}}\right)^{\beta_X}\right)^{\alpha_X} & 0 \leqslant \rho \leqslant \rho_{ped} \\ X_{sep} + \left(X_{ped} - X_{sep}\right)\left(\dfrac{1-\rho}{1-\rho_{ped}}\right) & \rho_{ped} \leqslant \rho \leqslant 1 \end{cases}. \tag{12}$$

In this study, we take the pedestal at normalised radius $\rho_{ped} = 0.94$, with the density and temperature profile exponents of $\alpha_n = 1.0$, $\beta_n = 2.0$, $\alpha_T = 1.45$, and $\beta_T = 2.0$. Note that Shafranov shift is ignored in PROCESS.

The density at the pedestal and separatrix are taken as fractions of the Greenwald density, n_{GW}: $n_{e,ped} = 0.85 n_{GW}$ and $n_{e,sep} = 0.5 n_{GW}$. The electron temperature at the pedestal,

Table 3. Summary of the fixed input parameters for the TF coils used in this study.

Parameter	Description	Value
n_{TF}	Number of TF coils	16
$t_{TF,case,plasma}$ (m)	Plasma-facing thickness of the TF coil casing at the inboard	0.06
$t_{TF,case,side}$ (m)	Sidewall thickness between the angled edge of the case trapezoid and the rectangularWP	0.05
$t_{TF,insert}$ (m)	Winding pack insertion thickness	0.01
$t_{TF,ins}$ (m)	Winding pack ground insulation thickness	0.008
$t_{CICC,ins}$ (m)	CICC turn insulation thickness	0.002
$D_{CICC,He}$ (m)	Diameter of the CICC spiral-wound helium coolant channel	0.01
$f_{CICC,He}$	Area fraction of coolant in the CICC	0.3
$\delta_{B,max}$	Peak toroidal field ripple at $R_0 + a$	0.006
$P_{nuc,TF}$ (MW)	Nuclear heating in the TF coil	0.013
$T_{TF,He,peak}$ (K)	Peak TF coil supercritical helium temperature	4.75
$T_{CS,He,peak}$ (K)	Peak CS coil supercritical helium temperature	4.75
$T_{TF,He}$ (K)	TF coil supercritical helium temperature	4.5
$T_{CS,He}$ (K)	CS coil supercritical helium temperature	4.5
ΔT_{TF} (K)	Temperature margin in the TF coil	1.5
ΔT_{CS} (K)	Temperature margin in the CS coil	1.5
$V_{TF,TFCFD}$ (kV)	Peak voltage in the TF coil during a TFCFD	10

Table 4. Summary of the fixed terms in the radial build used in this study.

Parameter	Description	Value
$t_{CS\rightarrow TF}$ (m)	Gap between the CS precompression structure and the TF coils	0.05
$t_{TF\rightarrow TS}$ (m)	Gap between the TF coil and the thermal shield	0.05
t_{TS} (m)	Thickness of the thermal shield (inboard and outboard)	0.05
$t_{TS\rightarrow VV}$ (m)	Gap between the thermal shield and the vacuum vessel	0.02
$t_{VV,inboard}$ (m)	Thickness of the inboard vacuum vessel	0.6
$t_{VV\rightarrow BB}$ (m)	Gap between the vacuum vessel and blankets (inboard and outboard)	0.02
$t_{BB,inboard}$ (m)	Thickness of the inboard breeding blanket	0.773
$t_{BB\rightarrow plasma}$ (m)	Gap between the blankets and the plasma (inboard and outboard)	0.225
$t_{BB,outboard}$ (m)	Thickness of the outboard breeding blanket	1.0
$t_{VV,outboard}$ (m)	Thickness of the outboard vacuum vessel	1.1

$T_{e,ped}$, is calculated following an EPED [32, 33] scaling, see equation (13) [34]

$$T_{e,ped} = 0.65 \times 2.16 \times \delta^{0.82} I_p^{0.26} R_0^{-0.39} \beta_N^{0.43} \kappa^{0.5} a^{0.88} \quad (13)$$

where β_N is the normalised ratio of plasma pressure to magnetic energy density.

A correction factor of 0.65 is taken for the single null case. The electron temperature at the separatrix is taken as $T_{e,sep} =$ 0.1 keV. Ion temperature is assumed to be equal to electron temperature across the profile, i.e. $\theta_i \equiv T_i/T_e = 1$.

The q-profile is taken as a clamped parabola, assuming that sawteeth or flux pumping (see [35]) distribute the current in the core, when one might otherwise expect $q < 1.0$. In practice however, q_{95} is imposed, as is the safety factor at the core $q_0 = 1.0$.

The plasma core is assumed to be at thermal equilibrium, such that:

$$f_{P_\alpha} P_\alpha + P_{charged} + P_{ohmic} + P_{add} = P_{rad,core} + P_{syn} + P_{con} \quad (14)$$

where f_{P_α} is the fraction of alpha power trapped in the plasma, taken here as 0.95. P_{add} is the added power from heating and current drive, and P_{con} is the conduction-convection loss term, calculated as:

$$P_{con} = \frac{W_{th}}{\tau_E(P_{net})}. \quad (15)$$

The IPB98(y,2) scaling law is used for τ_E (see section 3.5 and equation (8)) with an imposed radiation-corrected H-factor of $H_{rc} = 1.1$ (see [2]), as this corresponds to an H-factor

$H \approx 1.0$. P_{net} is the net power delivered to the plasma, where P_{net} is: (14)

$$P_{net} = f_{P_\alpha} P_\alpha + P_{charged} + P_{ohmic} + P_{add} - P_{rad,core} - P_{syn} \tag{16}$$

where $P_{rad,core}$ are the losses to the heating power in the confinement scaling, assumed to be instantaneous.

Reaction rates for D-T and D-D fusion are calculated using the Bosch-Hale parameterisation for the Maxwellian reactivities [36]. D-He3 fusion is ignored.

The apparent helium particle confinement time is prescribed by an imposed ratio of helium to energy confinement times of $r_{\tau,He} \equiv \tau^*_{He}/\tau_E = 5.0$, which is then used to calculate the fraction of helium in the plasma, f_{He}.

The power crossing the separatrix required to access to H-mode is calculated with the Martin scaling [37], see equation (17).

$$P_{LH} = 0.0488 \overline{n_{e,20}}^{0.717} B_T^{0.803} S_{plasma}^{0.941} \tag{17}$$

where $\overline{n_{e,20}}$ is the line-averaged electron density in units of 10^{20} m^{-3} and S_{plasma} is the plasma surface area.

4.1.2. Impurities and radiation. The radiation-corrected H-factor is calculated using a core radius of $\rho_{core} = 0.75$ and a core radiation fraction $f_{rad,core} = 0.6$, as suggested in [2].

A constant tungsten impurity concentration of $c_W = 5 \times 10^{-5}$ is assumed. Xenon is used as the seeded core impurity, with the concentration c_{Xe} being used as a variable. The radiated power from impurities is calculated using volumetric radiative loss functions, L_Z in W m^{-3}, for each impurity species derived using results from the ADAS code [38] assuming coronal equilibrium, and include Bremsstrahlung, and line and recombination radiation, see equation (18). The density dependence of L_Z is weak and is ignored. Radiation outside the separatrix is not treated. More details can be found in [5]

$$P_{rad} = \int_\rho \sum_i n_i(\rho)\, n_e(\rho)\, L_{Z_i}(Z_i, T_e(\rho))\, V(\rho) \tag{18}$$

Synchrotron radiation is calculated using a formulation found in [39], from [40, 41], in which reflections are accounted for. Here we take the reflection coefficient from the wall as $f_{syn} = 0.6$.

The plasma effective charge is calculated as:

$$Z_{eff} = \sum_i c_i \langle Z_i(\langle T_e \rangle) \rangle^2 \tag{19}$$

with the average charge $\langle Z \rangle$ calculated at the average electron temperature again using results from the ADAS code over all ion species i. Note that $\langle Z \rangle^2$ is not equal to the mean squared charge $\langle Z^2 \rangle$, and this calculation should in fact be carried out as an integral over the plasma profile using the mean squared charged. Equation (19) results in a slight overestimate of Z_{eff}; however, the 'required' value could simply be achieved by increasing the concentrations of the seeded impurities to achieve the same result (the dilution effect being relatively small for low impurity concentrations).

The plasma resistance is calculated as [5, 42] :

$$R_{plasma} = 0.66 \times (4.3 - 0.6A) \times 2.15 \times 10^{-9} \frac{Z_{eff} R_0}{\kappa_{95} a^2 (T_e/10)^{3/2}} \tag{20}$$

where the 0.66 is a factor to match more detailed EU-DEMO calculations using ASTRA, and the second term is a neoclassical resistivity enhancement factor [43]. The loop voltage during the flat-top is then calculated as:

$$v_{loop} = f_{ind} I_p R_{plasma} \tag{21}$$

where f_{ind} is the fraction of the plasma current produced inductively. The effects of sawteeth are ignored.

4.1.3. Plasma shape. The aspect ratio, A, is one of the main 'free' parameters in tokamak design, and many past studies (including on EU-DEMO [44]) have investigated the effects of varying aspect ratio on performance.

For this study, where we want to reduce the technological challenges of the divertor and magnet systems, whilst increasing q_{95}, reducing A when compared to the EU-DEMO 2017 baseline (with $A = 3.1$) has already been found to be of interest [45].

The elongation at the 95th flux percentile, κ_{95}, has a strong influence on the performance of the plasma, and the maximum vertically stable elongation increases with decreasing A. A surrogate model for the maximum vertically stable elongation as a function of A and the stability margin, m_s, see equation (22) [46], using data from [47] (in which sub-optimally positioned passive conductive structures were used to calculate m_s, meaning that surrogate results should be conservative), was included in PROCESS.

$$\kappa_{95}(A, m_s) = \frac{18.84 - 0.87A - \sqrt{4.84A^2 - 28.77A + 52.52 + 14.74 m_s}}{7.37} \tag{22}$$

$m_s = 0.3$ is recommended in [48], and has been used previously for EU-DEMO [49]. Following the decision to adopt the ITER criteria [50] on more conservative vertical stabilisation for robust operation [51], in-vessel active stabilisation coils were included in EU-DEMO. As such, we have chosen $m_s = 0.2$ in this study.

The edge elongation, κ, is calculated as $\kappa = f_\kappa \kappa_{95}$, with $f_\kappa = 1.12$ in this case. The edge triangularity, and triangularity at the 95th percentile flux surface are set to $\delta = 0.5$ and $\delta_{95} = 0.333$.

The plasma volume, surface area, poloidal cross-sectional area, and poloidal perimeter are calculated using a simplified geometrical representation of the plasma poloidal cross-section, see [5].

4.1.4. Plasma current. The total plasma current is calculated as per equation (3), with the scaling term $\mathcal{S}$ taken as [42]:

$$\mathcal{S} = \frac{5}{2}\frac{1.17-0.65\epsilon}{\left(1-\epsilon^2\right)^2}\left(1+\kappa_{95}\left(1+2\delta_{95}^2-1.2\delta_{95}^3\right)\right) \quad (23)$$

where $\epsilon \equiv 1/A$.

The bootstrap current is calculated using the Sauter formulae [52, 53] integrated across the plasma profiles. Alternative formulae for the trapped particle fraction and ion and electron collision frequencies are used, following [20].

The normalised plasma internal inductance is calculated according to an empirical fit found in Wesson [54]:

$$l_i = \ln\left(1.65+0.89\left(q_{cyl}/q_0-1\right)\right) \quad (24)$$

where q_{cyl} is the equivalent cylindrical safety factor at the edge, which is taken as:

$$q_{cyl} = q_{95}\frac{\left(1-\epsilon^2\right)^2}{1.17-0.65\epsilon}. \quad (25)$$

4.1.5. Heating and current drive. In preparation for the G1 Gate Review, a decision was made to use only EC current drive (ECCD) for EU-DEMO.

The injected steady-state ECCD power is fixed at $P_{CD} = 40$ MW, with a EC heating power of $P_{heat} = 10$ MW.

A fixed value of normalised current drive efficiency was used $\gamma_{ECCD} = 0.3\ 10^{20}$ A W^{-1} m^{-2}, with a wall-plug efficiency of $\eta_{EC} = 0.4$.

The Ohmic heating power to the plasma is calculated as:

$$P_{ohmic} = f_{ind} I_p^2 R_{plasma}. \quad (26)$$

4.1.6. TF coils. The TF coil used in this study is similar to those used in previous EU-DEMO studies [3, 9], with many of the input values and assumptions particularly surrounding the superconductor and conduit/WP dimensions coming from detailed discussions with the magnet team, see table 3 and e.g. [55]. The inboard TF coil geometry is trapezoidal, with a curved inner edge. The TF coil casing is wedged, and not bucked. The number of TF coils is $n_{TF} = 16$. A single rectangular pancake-wound cable in conduit conductor (CICC) Nb_3Sn winding pack of 20 pancakes by 10 layers is assumed for the TF coil. Radial plates are not used.

The plasma-facing thickness of the TF coil casing at the inboard is set as $t_{TF,case,plasma} = 0.06$ m. The sidewall thickness (between the angled edge of the trapezoid and the rectangular winding pack) is taken as $t_{TF,case,side} = 0.05$ m. A winding pack insertion gap of $t_{TF,insert} = 0.01$ m and a ground insulation layer of $t_{TF,ins} = 0.008$ m is assumed.

The inboard TF coil case thickness, $t_{TF,nose}$, is a design variable. The conductor jacket thickness, $t_{TF,jacket}$, is also a design variable, for which a lower bound of 0.008 m is used, accounting for manufacturing considerations. The current per turn, $I_{TF,turn}$ is a variable, and is bound between 60 kA and 90 kA. A conduit insulation thickness of $t_{CICC,ins} = 0.002$ m is used. The diameter of the CICC spiral-wound helium coolant channel is $D_{CICC,He} = 0.01$ m, with a coolant fraction of $f_{CICC,He} = 0.3$ assumed across the CICC. The peak helium temperature is taken as $T_{TF,He} = 4.75$ K.

The peak toroidal field ripple (calculated at $R_0 + a$) is set to $\delta_{B,max} = 0.6$ % and is used to determine the position of the outer leg of the TF coil (based on a fit to some Biot-Savart calculations, see [5]). The position of the outer leg of the TF coil effectively determines the volume and stored energy of the TF coil, which is then used to calculate vertical force in the TF coil and the fraction of copper required in the event of a quench and TF coil fast discharge (TFCFD). The peak voltage during a TFCFD is taken as $V_{TF,TFCFD} = 10$ kV.

The nuclear heating in the TF coil is fixed for EU-DEMO studies, with $P_{nuc,TF} = 0.013$ MW, which is used in part to determine the parasitic loads for cryogenic cooling.

4.1.7. PF system. The poloidal field (PF) system is comprised of a single superconducting central solenoid (CS) and six superconducting PF coils. In PROCESS, the sole purpose of these coils is to provide the flux swing necessary for the operation of a pulsed machine.

Similarly to the TF coils, Nb_3Sn is chosen as the superconducting material. The CS coil thickness, t_{CS} is a design variable.

The PF coils are not designed in detail, and notional coils are positioned relative to the plasma in order to determine approximate equilibrium currents at the start and end of flat-top, and thereby calculate the contributions of the CS and PF to the poloidal flux balance, see appendix D for more detail.

4.1.8. Blanket and divertor. For EU-DEMO studies, very simplified blanket models and balance of plant tend to be used; relying on a wide set of detailed design studies to provide the input parameters necessary to evaluate the performance as accurately as possible.

As in previous studies, the inboard and outboard blanket thickness are inputs, taken here (as in [3, 9]) as $t_{BB,inboard} = 0.773\ m$ and $t_{BB,outboard} = 1.0\ m$. These values typically result in sufficiently high tritium breeding ratios (TBR) in detailed blanket design and Monte Carlo radiation transport studies for both HCPB and WCLL blankets over a range of different machine geometries, see e.g. [56]. Studies have also shown that the shielding of the vacuum vessel is also sufficient with these blanket thicknesses in the HCPB case [57, 58], which is likely to be more challenging from a shielding perspective. As such, the blanket design in PROCESS is essentially fixed.

In this study, we explicitly assume a WCLL breeder blanket—in contrast to previous EU-DEMO studies, where a HCPB blanket was assumed. This is not a design decision; the performance of the WCLL blanket in PROCESS in terms of $P_{el,net}$ is now much lower than that of the HCPB blanket (which was re-designed to have a lower pressure drop, see [12]), so a PROCESS design point with WCLL will also be able to accommodate a HCPB blanket and still meet the $P_{el,net}$ requirement. Following recent WCLL design studies [59], we take an energy multiplication factor of $e_{mult} = 1.2$.

The lifetime of EU-DEMO is presently still assumed to be dictated by the requirement to achieve a total fluence equivalent to 20 + 50 dpa in EUROfer at the outboard midplane behind the tungsten first wall [60]. In PROCESS, a simplified scaling to detailed neutronics studies on the previous design point (9.89 dpa fpy^{-1} for $P_{fus} = 1998$ MW, as per [12]) is used to estimate the quantity of full-power years required to reach $L_{dpa} = 70$ dpa:

$$L_{fpy} = \frac{L_{dpa} \times 1998}{9.89 \times P_{fus}}. \tag{27}$$

A single divertor with a solid angle fraction of $f_{div} = 0.115$ is taken, which is then used to determine the amount of nuclear power deposited in the divertor. Here, no penalty for H&CD systems or other non-blanket regions is taken, such that $f_{BB} = 0.885$. A small fraction of nuclear power is assumed to reach the vacuum vessel (<1%) and TF coils ($P_{nuc,TF}$, see section 4.1.6).

4.1.9. Radial build. The radial build for EU-DEMO is largely fixed, with only four quantities actually allowed to vary. These are: the CS coil thickness, t_{CS}, inboard TF coil thickness t_{TF}, the plasma minor radius, a, and the position of the outer leg of the TF coil. The fixed quantities are input thicknesses and gaps between various components (vacuum vessel, thermal shields, breeding blanket, etc). A full account of the fixed radial build values used in this study is given in table 4.

4.1.10. Electrical power balance. Given that $P_{el,net}$ is an important value for EU-DEMO design, an attempt is made in PROCESS design studies to account for all major parasitic loads, see equation (28):

$$\begin{aligned} P_{el,net} = & P_{el,tot} \\ & - P_{el,BB,pump} - P_{el,div,pump} - P_{el,HCD} \\ & - P_{el,TF} - P_{el,PF} - P_{el,cryoplant} \\ & - P_{el,building} - P_{el,misc}. \end{aligned} \tag{28}$$

The total electrical power is calculated as $P_{el} = \eta_{th} P_{tot,thermal}$ where $P_{tot,thermal}$ is the thermal power in the blankets and divertors (ignoring differences in coolant output temperatures). For a WCLL blanket, we have taken $\eta_{thermal} = 0.316$ as representative of more dedicated studies [14, 61]. Energy multiplication is applied to the nuclear power deposited in the blankets only.

The electrical pumping power for the BB, $P_{el,BB,pump}$, and divertor, $P_{el,div,pump}$, coolant loops are calculated in a simplified form:

$$P_{el,pump} = \frac{1}{\eta_{pump,electrical}} \frac{f_{pump}}{1 - f_{pump}} P_{thermal} \tag{29}$$

where f_{pump} is a fraction of the incident thermal power to be pumped. Here we have taken $f_{BB,pump} = 0.0111$ for a WCLL blanket and $f_{div,pump} = 0.05$, with an electrical efficiency of $\eta_{pump,electrical} = 0.9$.

The electrical power for the ECCD dominates the parasitic load and is taken as $P_{el,HCD} = (P_{CD} + P_{heat})/\eta_{EC}$, giving 125 MWe in our case. The EC heating power ($P_{heat} = 10$ MW) is intended primarily for control purposes, and is not expected to be required continuously. Nevertheless, it is accounted for in the above as a steady-state parasitic load.

The building electrical power $P_{el,building}$ is calculated as a power per floor area, $f_{el,area} = 1.5 \times 10^{-4}$ MW m^{-2} multiplied by the floor area, which is a weak function of R_0, A, κ, etc and various assumptions regarding the sizes of the many auxiliary buildings.

In this study, miscellaneous parasitic electrical loads (e.g. T plant, control room, diagnostics, etc) are input via $P_{el,misc}$, which we take as 65 MW, as in previous EU-DEMO studies [3, 9].

4.2. Design constraints

4.2.1. Divertor protection. Following [10], $P_{sep}B_T/q_{95}AR_0$ was used as a divertor protection criterion in the G1 baseline design. For the G1 baseline, a maximum value of $P_{sep}B_T/q_{95}AR_0 = 9.2\,\mathrm{MW \cdot T\,m^{-1}}$ was used [3, 4]. In subsequent years, off-normal load cases were studied more seriously in EUROfusion, and it was accepted that LODEs must be considered as possible off-normal events [62]. Divertor target sweeping is the chosen operational mitigation strategy for such events, and is able to handle effective, transient divertor outer target heat fluxes of up to $\dot{q}_{div,outer} \approx 60$–$70$ MW m^{-2} [62].

Performing the same calculation as in [62], the EU-DEMO 2017 baseline reaches $\dot{q}_{div,outer} \approx 83$ MW m^{-2}.

As such, we have chosen to keep the value of $P_{sep}B_T/q_{95}AR_0 \leqslant 6.0\,\mathrm{MW \cdot T\,m^{-1}}$ in this study, which corresponds approximately to $\dot{q}_{div,outer} \approx 50$ MW m^{-2} during re-attachment.

Furthermore, in keeping with our desire to have robust margins in terms of plasma physics uncertainties, we also choose to account for the effects of a potential reduction in q_{95} from the reference value in the divertor protection constraint, see equation (30)

$$(P_{sep}B_T/q_{95}AR_0)^* \equiv \frac{q_{95}}{(q_{95})^*} P_{sep}B_T/q_{95}AR_0 \leqslant 6.0\ \mathrm{MW \cdot T\,m^{-1}}. \tag{30}$$

4.2.2. Plasma stability. The ratio of thermal plasma pressure to magnetic energy density, $\beta_{thermal}$, is calculated as:

$$\beta_{thermal} = 2 \times 10^3 \mu_0 e \frac{(\langle n_e \rangle + \langle n_i \rangle) \langle T_e \rangle_n}{\sqrt{B_T^2 + \langle B_P \rangle^2}} \tag{31}$$

where $\langle T_e \rangle_n$ is the density-weighted electron temperature in keV, remembering that $T_e/T_i = 1$. The fast alpha contribution to beta is calculated using a scaling to $\beta_{thermal}$ [5], slightly

modified from [63]:

$$\beta_{ft} = 0.26 \left(\frac{\langle n_i \rangle}{\langle n_e \rangle} \right)^2 \sqrt{0.1 \langle T_e \rangle_n - 0.6}\, \beta_{thermal}. \tag{32}$$

A Troyon-like limit is applied to the ratio of thermal pressure to magnetic pressure (i.e. excluding fast alphas):

$$\beta_{thermal} = \beta - \beta_{ft} \leqslant 0.03 \frac{I_p}{aB_T} \tag{33}$$

where β is the ratio of the total plasma pressure to magnetic energy density, and is a variable in the optimisation problem.

4.2.3. Access to H-mode. The power for accessing H-mode is calculated with the Martin scaling [37], see equation (17).

We take $f_{LH} \equiv P_{sep}/P_{LH} \geqslant 1.1$ as the factor for epistemic uncertainties associated with access to H-mode, in keeping with previous EU-DEMO studies [3, 9].

Technically, to be in keeping with our approach, we should account for the density dependency here too:

$$(f_{LH})^* \equiv \left(\frac{q_{95}}{(q_{95})^*} \right)^{0.717} f_{LH} \tag{34}$$

however this effect is relatively minor compared with the substantial confidence interval of the Martin scaling. $f_{LH} = 1.1$ corresponds to a margin of $\Delta P_{LH} = 0.091$ whereas the root-mean-squared error of the Martin scaling is 30.8% [37].

4.2.4. Superconducting coil constraints. As in previous EU-DEMO design studies, a Bottura-Bordini parameterisation [64] with a fit to the Nb_3Sn WST strand [55] is used to calculate the critical current densities in the TF and CS, $j_{TF,crit}$ and $j_{CS,crit}$, as a function of the temperature, field, and strain. A residual manufacturing strain of $\epsilon_{residual} = -0.5\%$ is taken in both the TF and CS windings. The current densities in the superconductors are then constrained as:

$$\begin{aligned} j_{TF} &\leqslant j_{TF,crit} \\ j_{CS} &\leqslant j_{CS,crit} \end{aligned} \tag{35}$$

where $j_{TF,crit}$ and $j_{CS,crit}$ are evaluated at the peak toroidal magnetic field in the TF, $B_{T,TF}$, and at the current-sharing temperature: $T_{cs} = T_{He,peak} + \Delta T$, with a temperature margin of $\Delta T = 1.5$ K. No peak field constraints are applied to the superconductor; the maximum field is indirectly constrained by the choice of superconducting parameterisation, ΔT, and the space available for the winding pack, etc.

4.2.5. Coil and vacuum vessel stress constraints. The TF coils are sized in PROCESS accounting for the stresses in the nose and winding pack conductor jacket, as calculated at the inboard midplane using a simplified two-layer cylindrical plane stress model with smeared structural properties which compares well with finite element analyses [65]. SS316-LN is chosen as the structural material for both TF nose and conductor jacket. Normally, we would use a Tresca stress limit of 660 MPa for the stress in the TF (2/3 of σ_y), but we use 580 MPa, taking into account stress concentration factors from more detailed 3D studies of TF coil structures. A more complete description of these constraints can be found in appendix B.

The hoop stress in the CS coil, σ_{CS}, is constrained to be below 660 MPa, again for SS316-LN, but with no stress concentration factors. This constraint in fact tends to be dominated by the application of the new fatigue constraints for our design problem, see the next subsection

$$\begin{aligned} \sigma_{TF,case} &\leqslant 580 \text{ MPa} \\ \sigma_{TF,WP} &\leqslant 580 \text{ MPa} \\ \sigma_{CS} &\leqslant 660 \text{ MPa}. \end{aligned} \tag{36}$$

The stress in the vacuum vessel (VV) shell during a TF coil fast discharge (TFCFD), $\sigma_{VV,TFCFD}$ is constrained to be below 93 MPa, again following detailed studies [66]. This constraint has the effect of increasing the discharge time constant of the TF coils during a quench, τ_{TFCFD}, thereby increasing the quantity of copper required in the winding pack.

4.2.6. CS fatigue. Fatigue was found to be a design-driving issue in the EU-DEMO CS [67, 68]. Following [67], a Paris law [69] crack growth model was implemented in PROCESS of the form:

$$\frac{dA_{crack}}{dn_{cycles,CS}} = C \delta K^m \tag{37}$$

describing the growth of the crack with the number of cycles, $n_{cycles,CS}$, where C and m are material properties and δK is a stress intensity factor range, which is related to the cyclic stress and the assumed geometry of the structure and crack. Equation (37) is solved for $n_{cycles,CS}$, and a constraint is applied such that:

$$n_{cycles} \leqslant n_{cycles,CS} \tag{38}$$

where n_{cycles} is the required number of cycles to reach L_{dpa}, see appendix C for a full description.

The ITER material of choice for the CS conductor jacket, JK2LB, exhibits superior fatigue performance [70] but the ITER experience has shown this comes at the cost of significant manufacturing and quality assurance complications (see e.g. [71]). A decision was taken to use SS316-LN for the CS conductor jacket, in keeping with the general conservative EU-DEMO philosophy and the return on experience from ITER.

4.3. Specification of the parameter space

For this latest iteration of the EU-DEMO design point, we have chosen to use $q_{95,min} = 3.3$, aiming for a hybrid regime of operation, and addressing point (ii) of the G1 Gate Review recommendations (see section 1).

We have also decided to re-visit the stakeholder requirement for $P_{el,net} \in [300\text{–}500]$ MWe, now that we decided to maintain P_{fus} at a nominal value.

These considerations, in combination with some preliminary design exploration studies have led us to study the following parameter space, $\mathbf{\Omega}$, in more detail:

$$\mathbf{\Omega} = \begin{cases} A & \in [2.7 - 2.9] \\ R_0 & \in [8.5 - 8.9] \text{ m} \\ q_{95} & \in [3.3 - 3.8] \\ P_{el,net} & \in [300 - 500] \text{ MWe} \end{cases} . \tag{39}$$

We define a point in this space as:

$$\mathbf{y} = \{A, R_0, q_{95}, P_{el,net}\} . \tag{40}$$

4.4. Design optimisation problem

For the optimisation objective, we have chosen to maximise the machine pulse length, τ_{pulse} (see calculation in appendix D), for a prescribed major radius, departing from the previous G1 philosophy of minimising R_0. This decision has two principal motivations: firstly, it makes little sense to use R_0 as a minimisation objective for machine size when varying A, and secondly, we have decided to fix machine geometry and vary instead the performance of the reactor. This latter choice comes from a desire to speed up turnaround of detailed studies. Fixing machine geometry allows distributed teams to preserve CAD models, meshes, finite element meshes, Monte Carlo radiation transport meshes and geometries, equilibria and plasma meshes, etc.

Note that, again, we account for a potential reduction of q_{95} in the pulse length, see equation (41):

$$\left(\tau_{pulse}\right)^* = \frac{\left(q_{95}\right)^*}{q_{95}} \tau_{pulse} . \tag{41}$$

As q_{95} is reduced, the plasma current will also increase, as such reducing the pulse length for a fixed loop voltage and CS design. Equation (41) is, in fact, a simplification of the true poloidal flux balance which ultimately determines the pulse length, as it ignores the increase in the resistive flux consumption and the positive contribution of the poloidal flux stored in the vertical field—both of which vary with I_p.

$$\begin{aligned} \mathbf{x}^* = \underset{\mathbf{x}}{\text{minimise}} : & -\left(\tau_{pulse}\right)^* \\ \text{subject to} : & \\ \mathbf{x} &\succcurlyeq \mathbf{x_{min}} \\ \mathbf{x} &\preccurlyeq \mathbf{x_{max}} \\ A,\ R_0,\ q_{95},\ P_{el,net} &= \mathbf{y} \\ \left(P_{sep} B_T / q_{95} A R_0\right)^* &\leqslant 6.0 \text{ MW} \cdot \text{T m}^{-1} \\ \beta_{thermal} &\leqslant 0.03 \times 10^{-6} \frac{I_p}{a B_T} \\ \sigma_{TF,case} &\leqslant 580 \text{ MPa} \\ \sigma_{TF,WP} &\leqslant 580 \text{ MPa} \\ \sigma_{CS} &\leqslant 660 \text{ MPa} \\ \sigma_{VV,TFCFD} &\leqslant 93 \text{ MPa} \\ j_{TF} &\leqslant j_{TF,crit} \\ j_{CS} &\leqslant j_{CS,crit} \\ n_{cycles} &\leqslant n_{cycles,CS} \\ &\dots \end{aligned} \tag{42}$$

where the solution vector $\mathbf{x}$ and its bounds are:

$$\mathbf{x_{min}} \preccurlyeq \mathbf{x} \preccurlyeq \mathbf{x_{max}} \equiv \left\{ \begin{array}{rcl} 0 \leqslant & B_T & \leqslant 20 \\ 0 \leqslant & \langle T_e \rangle & \leqslant 150 \\ 0 \leqslant & \langle n_e \rangle & \leqslant \infty \\ 0 \leqslant & \beta & \leqslant \infty \\ 0 \leqslant & f_{GW} & \leqslant 1.2 \\ 1.1 \leqslant & f_{LH} & \leqslant \infty \\ 0 \leqslant & c_{Xe} & \leqslant \infty \\ 0.3 \leqslant & t_{TF} & \leqslant \infty \\ 0 \leqslant & t_{TF,case} & \leqslant \infty \\ 0.5 \leqslant & f_{Cu,TF} & \leqslant 0.94 \\ 6 \times 10^4 \leqslant & I_{TF,turn} & \leqslant 9 \times 10^4 \\ 0.008 \leqslant & t_{TF,jacket} & \leqslant \infty \\ 0 \leqslant & \tau_{TFCFD} & \leqslant \infty \\ 0.1 \leqslant & t_{CS} & \leqslant \infty \\ 0.1 \leqslant & R_{CS,in} & \leqslant \infty \\ 0 \leqslant & f_{SS316,CS} & \leqslant \infty \\ 0 \leqslant & j_{CS} & \leqslant \infty \\ & \dots & \end{array} \right\} . \tag{43}$$

The ellipsis in equations (42) and (43) indicate constraints, variables and bounds that are for consistency (e.g. radial build, conservation of energy, $n_{e,core} > n_{e,ped}$, etc) and/or specific to implementation details in PROCESS (e.g. so-called f-values) and not relevant to the problem formulation described here.

This study was carried out with a slightly modified version of PROCESS 2.4.0, rather than the open-source version [72], which was necessary to preserve some model formulations that were specifically developed for EUROfusion but could

not be released open-source for intellectual property reasons. The optimisation was performed using the VMCON gradient-based algorithm for non-linearly constrained problems [73].

5. Results

5.1. Design space results

Taking the Cartesian product of a linear discretisation of the manifold in equation (39), equation (42) is solved $\forall\, \mathbf{y} \in \mathbf{\Omega}$. A sub-set of the results for this operation are shown in figures 1–3, where the results are shown in $\{q_{95}, P_{el,net}\}$ space, for three combinations of $\{A, R_0\}$. In these figures, the filled contours correspond to the values of $(\tau_{pulse})^*$ and the white regions indicate where no feasible solutions were found. The red lines correspond to $P_{el,net} = 350$ MWe and the blue lines correspond to $(\tau_{pulse})^* = 2$ h.

These design spaces all exhibit the same behaviour, with the following constraints and bounds reached in all points:

$$\begin{aligned} \left(P_{sep}B_T/q_{95}AR_0\right)^* &= 6.0\ \mathrm{MW}\cdot\mathrm{T\,m^{-1}} \\ \sigma_{TF,case} &= 580\ \mathrm{MPa} \\ j_{TF} &= j_{TF,crit} \\ j_{CS} &= j_{CS,crit} \\ n_{cycles} &= n_{cycles,CS} \\ f_{GW} &= 1.2 \\ t_{TF,jacket} &= 0.008\ \mathrm{m}. \end{aligned} \tag{44}$$

The transition from feasible (filled contours) to infeasible (white) space is generally well-described by the inability to find solutions at the conditions listed in equation (44) with, additionally, $f_{LH} > 1.1$. This can be interpreted as the intersection of two constraints:

$$\begin{aligned} f_{LH} &\propto P_{sep}B_T^{-0.803} \geqslant 1.1 \\ P_{sep}B_T/q_{95}AR_0 &\propto P_{sep}B_T \leqslant 6.0\ \mathrm{MW}\cdot\mathrm{T\,m^{-1}} \end{aligned} \tag{45}$$

as all terms other than P_{sep} and B_T are fixed or constrained elsewhere. Sharp angles in the transitions in figures 2 and 3 are due to the finite discretisation of the space.

In each of figures 1–3, the radial build is fixed from the outer radius of the inboard TF coil right up to the outboard vacuum vessel. The only radial build variables are therefore the thickness of the TF and CS coils. The increasing pulse length with decreasing $P_{el,net}$ and q_{95} is because at lower P_{fus} and at lower q_{95}, less toroidal field is required. A lower B_T in turn, means a thinner TF coil, meaning the outer CS radius is larger for the same R_0, leading to higher achievable CS flux and longer τ_{pulse}.

Note that a higher ΔH, i.e. a higher q_{95}, is 'detrimental' to overall performance in terms of $P_{el,net}$. For example, on the blue line in figure 1 ($A = 2.7$, $R_0 = 8.7$ m, $(\tau_{pulse})^* = 2$ h), we see that a design point at $q_{95} = 3.6$ can produce $P_{el,net} \approx 350$ MWe, whereas at $q_{95} = 3.3$, $P_{el,net} > 500$ MWe would be possible. This is not surprising, as in fixed geometry and at constant f_{GW}, $\overline{n_e} \propto I_p \propto q_{95}^{-1}$ (see equation (3)); and as we saw in section 3.3 and appendix A, P_{fus} scales strongly with I_p and n_e. The second case corresponds to $\Delta H = 0$ (as in previous EU-DEMO baselines [3, 8]), and something that we have sought to address here, in line with the G1 Gate Review recommendations [7].

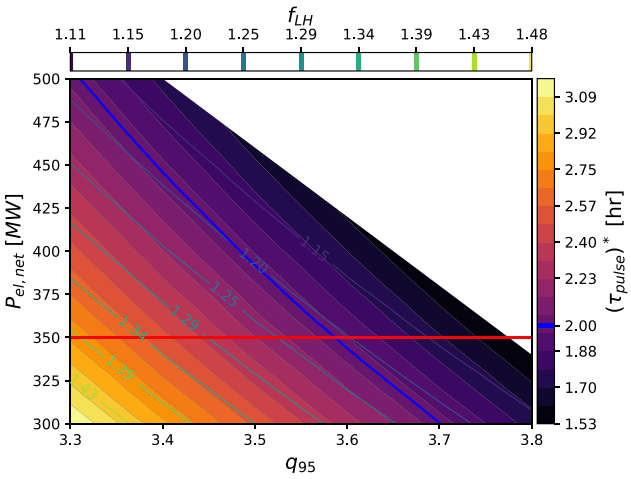

Figure 1. Design space for $A = 2.7$, $R_0 = 8.7$ m.

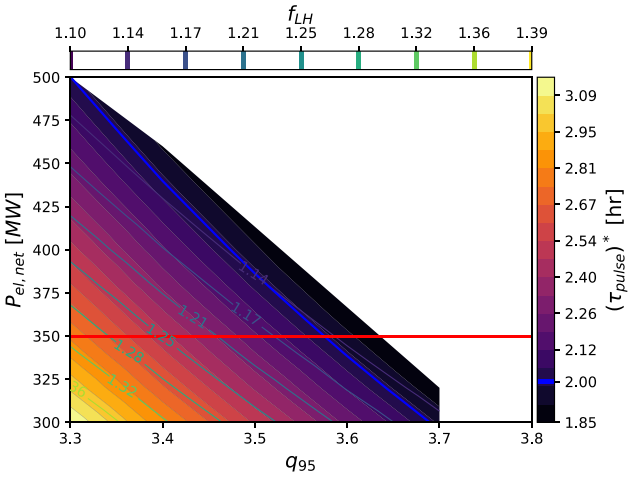

Figure 2. Design space for $A = 2.8$, $R_0 = 8.6$ m.

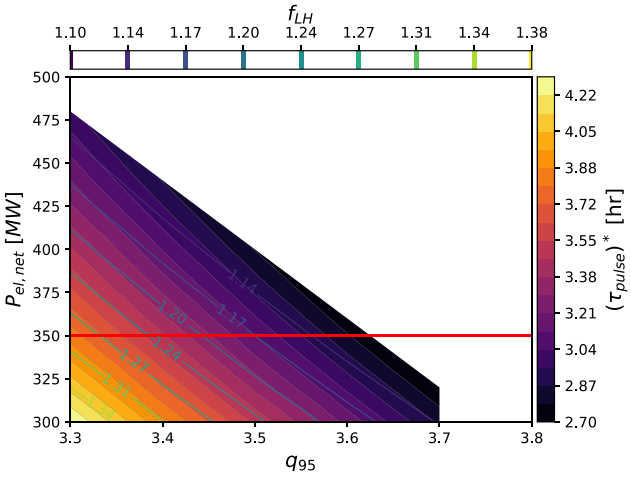

Figure 3. Design space for $A = 2.9$, $R_0 = 8.8$ m.

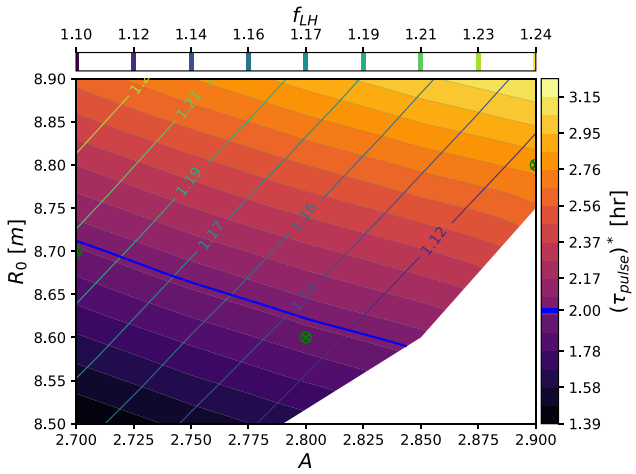

Figure 4. Design space for $q_{95} = 3.6$, $P_{el,net} = 350$ MWe.

5.2. Selection of a design point

Previous EU-DEMO design points have sought to meet the stakeholder requirements of $P_{el,net} \in 300$–500 MWe by setting the target net electrical power in PROCESS as $P_{el,net} = 500$ MWe, with the rationale that if fusion power were lower than predicted then the net electric power output would still hopefully be $P_{el,net} > 300$ MWe. Now that we explicitly include a margin for confinement uncertainties, we no longer need to have such a large margin in net electric power. Clearly, for the same physics and technology, a reactor that produces 300 MWe will have a lower capital cost than one which produces 500 MWe. Nevertheless, other uncertainties (e.g. in terms of parasitic loads) must still be accounted for. Based on the results presented in the previous section, and acknowledging our imperfect knowledge and the simplicity of the PROCESS systems code, we have decided to choose design points at $P_{el,net} = 350$ MWe. This gives us a margin on the net electric power, $\Delta P_{el,net} = 50$ MWe, on top of a margin for confinement uncertainties.

As can be seen from figures 1–3, the lower the net electric power, the higher the q_{95} for a given τ_{pulse}. We have decided to choose $q_{95} = 3.6$, as this will provide the largest ΔH, whilst still more-or-less satisfying $(\tau_{pulse})^* \geqslant 2$ h in the three combinations of A and R_0 shown above.

Figure 4 shows the $\{A, R_0\}$ design space at $q_{95} = 3.6$, and $P_{el,net} = 350$ MWe. The green markers indicate the locations of three candidate design points, for which a sub-set of output parameters are shown in table 5.

These design points, all at $q_{95} = 3.6$, are also equivalent in terms of ΔH, and $P_{sep}B_T/q_{95}AR_0$. The point at $A = 2.7$ performs better in terms of TF coils, with a lower peak field, $B_{T,TF}$, and lower stored magnetic energy $E_{TF,stored}$, and in terms of f_{LH}, but is substantially larger than the other two points, which perform similarly in terms of plasma volume, V_{plasma}. In terms of remote maintenance, no constraints were implemented in PROCESS, despite there being some indication that lower aspect ratio is worse [44, 74]. In the context of choosing one of the three points in table 5, it was felt that the shallow minimum of plasma surface area, S_{plasma}, at $A = 2.8$ (as an ersatz for the volume of a breeding blanket) would be the easiest to maintain. Despite this minimum being very shallow, and although the point at $A = 2.9$ performs much better in terms of τ_{pulse}, the point at $A = 2.8$ was chosen on account of it having the lowest R_0.

Table 5. Design points at $q_{95} = 3.6$, $P_{el,net} = 350$ MWe.

Parameter	$A = 2.7, R_0 =$ 8.7 m	$A = 2.8, R_0 =$ 8.6 m	$A = 2.9, R_0 =$ 8.8 m
A	2.7	2.8	2.9
R_0 (m)	8.7	8.6	8.8
B_T (T)	4.13	4.39	4.56
$B_{T,TF}$ (T)	10.02	10.37	10.36
$E_{TF,stored}$ (GJ)	104.1	109.2	118.0
I_p (MA)	19.64	18.79	18.25
f_{LH}	1.20	1.13	1.11
$(\tau_{pulse})^*$ (h)	1.96	1.93	2.79
τ_{pulse} (h)	2.14	2.11	3.05
V_{plasma} (m^3)	3132	2805	2791
S_{plasma} (m^2)	1593	1499	1512

5.3. Comparison with previous EU-DEMO design points

The lack of margin for physics uncertainties in the EU-DEMO 2017 baseline [3] has already been considered, and was addressed in a separate PROCESS design point which was subsequently used by the physics and magnet teams for their studies (a.k.a. EU-DEMO 2018 physics) [4, 9]. This design point followed the same philosophy as presented here: higher q_{95} for MHD stability and margin on uncertainties. However, as this design point was at $A = 3.1$, the only real scope for increasing q_{95} was to increase B_T, see table 6. This design point was subsequently found to be challenging from the perspective of the TF coils, and was in any case identical to the EU-DEMO 2017 baseline in terms of divertor challenge criterion. Furthermore, in reducing q_{95}, the EU-DEMO 2018 physics design point would have violated the divertor protection criterion considered.

So whilst the EU-DEMO 2018 physics design point achieves a high ΔH, more technical challenge was imparted to the divertor and magnets. With the proposed design point, we achieve a lower margin in terms of ΔH, but with considerably lower divertor heat loads (40% reduction in $P_{sep}B_T/q_{95}AR_0$), thanks to the lower A.

The choice of a WCLL blanket, and the use of the most recent estimates for pumping fraction, e_{mult}, and $\eta_{thermal}$ is a more pessimistic set of assumptions than was used in the previous design points, which somewhat unfairly accentuates the comparison in terms of $P_{el,net}$. Were an HCPB blanket to be assumed, with all the latest estimates in terms of e_{mult}, $\eta_{thermal}$, and coolant pressure drop, etc then the EU-DEMO 2024 proposal would reach $P_{el,net} \approx 420$ MWe, see appendix E.

Note that in [45], an EU-DEMO design point at $A = 2.8$ and $R_0 = 7.95$ m was proposed. The discrepancy between this result and the results presented in this work can be largely attributed to the use of different tools (PROCESS was not used in [45]) and input assumptions (e.g. a lower q_{95}, higher allowable

Table 6. Comparison of the previous EU-DEMO design points with the present proposal.

Parameter	EU-DEMO 2017 baseline [3, 4]	EU-DEMO 2018 physics [4, 9]	EU-DEMO 2024 proposal
R_0 (m)	8.94	9.00	8.60
A	3.1	3.1	2.8
B_T (T)	4.89	5.86	4.39
$B_{T,TF}$ (T)	10.61	12.50	10.37
n_{TF}	16	16	16
I_p (MA)	19.07	17.75	18.79
κ_{95}	1.65	1.65	1.74
δ_{95}	0.33	0.33	0.33
q_{95}	3.00	3.89	3.60
$q_{95,min}$ [a]	3.00	3.30	3.30
H_{rc}	1.1	1.1	1.1
H	0.99	0.98	0.99
ΔH [a]	0.0	0.0–0.198[b]	0.110
P_{fus} (MW)	1998	2012	1652
$P_{el,net}$ (MWe)	500	500	350
τ_{pulse} (h)	2.0	2.0	2.11
$\langle T_e \rangle$ (keV)	12.80	12.49	10.93
$T_{e,ped}$ (keV)	5.5	3.7	4.2
f_{GW}	1.2	1.2	1.2
β_N (%mT MA^{-1})	2.889	2.483	2.747
Z_{eff}	2.18	2.16	2.12
$P_{sep}B_T/q_{95}AR_0$ (MW $\cdot$ T m^{-1})	9.2	9.2	5.5
C_{Ejima}	0.3	0.3	0.2
e_{mult}	1.27	1.27	1.20
$\eta_{thermal}$	0.375	0.375	0.316

[a] Values calculated retrospectively.
[b] 0.0–0.198 for $P_{sep}B_T/q_{95}AR_0 = 9.20$–$9.94 \geqslant 9.20\,\mathrm{MW \cdot T\,m^{-1}}$.

Table 7. Zeroth order parameter variation in the worst-case confinement.

Parameter	Nominal case	$(\cdot)^*$ case
q_{95}	3.6	3.3
H	0.99	0.88
ΔH	0.11	0
τ_{pulse} (h)	2.11	1.93
$P_{sep}B_T/q_{95}AR_0$ (MW $\cdot$ T m^{-1})	5.5	6.0
f_{LH}	1.13	1.06
I_p (MA)	18.79	20.51
$\langle n_e \rangle$ (10^{19} m^{-3})	6.87	7.49

stresses in the TF nose and VV during a TFCFD, etc). The general trends we find herein, however, are similar to those found in [45].

5.4. $A = 2.8$ design point at 'worst-case' confinement

In accordance with the approach outlined in section 3.4, machine geometry, B_T, and P_{fus} are held constant. In table 7 we present the values of certain plasma parameters in the 'worst-case' confinement that we assume we can mitigate by $q_{95} \rightarrow q_{95,min}$. The values in the worst-case are calculated following the approach outlined in section 3.4, and are not the results of a PROCESS run.

Note that $(f_{LH})^* = 1.06 < 1.1$, which was discussed in section 4.2.3.

6. Discussion

6.1. A narrow view of uncertainties

Here, our efforts centre around the encapsulation of epistemic uncertainties in plasma confinement in terms of a margin on q_{95}. This is in reality a relatively limited perspective on epistemic uncertainties in plasma physics. In terms of known uncertainties, we explicitly relate the margin in q_{95} to H in section 3.5 and ignore the effect of varying q_{95} on P_{LH}.

Whilst our approach is suitable for treating underperformance in terms of P_{fus} more generally than just 'low H', it is quite likely that the compound effects of accounting for the uncertainties in confinement quality (i.e. H) *and* H-mode access (i.e. f_{LH}) require more margin in terms of q_{95}, and potentially a more serious treatment altogether. This is particularly important given that P_{sep} to a large extent drives the divertor heat loads, which are design-driving if one considers LODEs (as we do here).

Furthermore, the results presented herein rest heavily on the use of the IPB98(y,2) [1] and Martin and Takizuka [37] scaling laws, leveraging dependencies in n_e, I_p, and B_T in particular. These scaling laws have large root-mean-squared errors (in practical engineering terms), as do alternative scalings. The

choice of scaling laws has a dramatic impact on the results, and it is misleading to assume that a certain margin on a value calculated via a scaling law being within the RMSE means that a design point is 'robust'. It is only robust within the context of the assumptions made; i.e. that the scaling law and the associated extrapolation is valid. Ultimately, validation of scaling assumptions in $Q > 5$ experiments, supported by dedicated burning plasma modelling, is paramount.

6.2. Design implications of $q_{95} \rightarrow q_{95,min}$

Whilst in this approach, we have attempted to 'insulate' some key systems from the epistemic uncertainties in the plasma (TF coils, blankets, balance of plant, remote maintenance, etc), reducing q_{95} in an operational scenario whilst attempting to maintain P_{fus} at a nominal value implies changing I_p and n_e, and indeed virtually all plasma integral quantities and profiles. In reality, the situation will be far more complex than the simplified approach outlined in section 3.4, and requires modelling at higher fidelity in order to better characterise the impact.

It is clear, however, that such modifications to the reference operational scenario will affect various reactor sub-systems in many predictable ways, which can already be accounted for in the conceptual design stage.

In terms of normal operation at $q_{95} = (q_{95})^*$, some systems will need to be over-dimensioned in order to cope with the worst-case:

(i) The higher plasma density will require a higher fuelling rate, implying that pumping and fuelling systems must be designed accordingly.
(ii) The actual ECCD efficiency, $\gamma_{ECCD} \propto Z_{eff} n_e^{3/2} T_e^{-1}$, is likely to reduce, meaning that more gyrotrons will need to be installed than would be required for $q_{95} = 3.6$.
(iii) The poloidal field system will have to be designed with the higher plasma current, such that some PF coils will likely have to produce slightly larger currents in normal operation.
(iv) Diagnostic and control systems likely need to be designed considering the full potential range of variation in plasma parameters for $q_{95} \rightarrow (q_{95})^*$, although this may not be much more challenging than what is already required for a full plasma pulse.

Importantly, the increase in I_p also has consequences in terms of off-normal operation, such as:

(i) Off-normal events such as runaway electron beams, vertical displacement events, and disruptions are likely to happen slightly faster[12].
(ii) Larger electromagnetic loads on in-vessel components during disruptions, vertical displacement events, etc.
(iii) The higher density also means that the plasma mass is slightly higher, such that contact with limiters or the first wall will be worse than in the nominal case.

[12] Although some of these events are so catastrophic that the outcomes are likely to be the same in terms of investment protection.

These effects can to some extent be described as minor but for consistency, and with a particular view to making robust assumptions for safety load cases and licensing, the case at $(q_{95})^*$ should be considered even during conceptual design.

6.3. A 'flat' design space makes for difficult decisions

The specification of the optimisation objective and constraints was the subject of much internal debate. Ideally, of course, the objective function would be the minimisation of capital cost. The commonly used ersatz of R_0 is not appropriate when varying aspect ratio. Ultimately, we settled on the maximisation of the pulse length, subject to a variety of technological and physical constraints. The values of the constraints are implicitly used as metrics to reduce complexity and cost. Indeed, we are 'drawn' to low A because of the beneficial effects in terms of reduced divertor heat loads and increased margin on confinement, despite neither being in the objective function.

The resulting design space is dominated by the divertor constraint which effectively determines the maximum power that can cross the separatrix for a given q_{95}. The variation of the feasible solutions in this space is relatively small, and the final choice of the reference design point was ultimately made following a series of step-wise decisions comparing values of decreasing importance (pulse length, toroidal field, plasma volume, blanket volume).

This methodology is 'human-centric' and based primarily on progressively converging upon a consensus. From a purely technical standpoint, we would probably have been better served by a multi-criteria decision matrix or analytical hierarchy process which could have been incorporated as the objective function in the optimisation problem. From a sociological standpoint, however, this would have forced us to take many abstract decisions in a vacuum devoid of context, complicating the process of developing a technical consensus, and ultimately obfuscating the decision-making process.

6.4. Conservative choices with an eye on the future

For this proposed baseline revision for EU-DEMO, we have made many conservative decisions on technologies, materials, and input values with a view to producing a robust design point. However, we intend to investigate some potentially beneficial modifications:

(i) N50-H [75] as the structural material for the TF coil case and conduit jacket, which could potentially increase the allowable stress in the TF coil and reduce the width of the TF coil for the same B_T.
(ii) JK2LB [71] as the structural material for the CS coil conduit jacket as it exhibits superior fatigue properties. Manufacturing difficulties and the ROI from ITER have so far dissuaded us from using it, but if the benefits are high enough, we could change our minds.
(iii) Lower inboard VV and BB thicknesses, $t_{VV,inboard}$ and $t_{BB,inboard}$, by improving the designs of the VV and

inboard blanket, maintaining the same nuclear shielding and breeding criteria.

These modifications may be incorporated as future revisions to this proposed baseline, in which the benefits may be applied to any of: machine geometry, performance, and/or margin.

6.5. Implications for commercialisation strategies

Uncertainties in the performance of reactor-scale burning plasmas will certainly have an effect on the design and construction of first-of-a-kind (FOAK) fusion power plants. The design strategy proposed herein is intended for use on such FOAK plants, where the uncertainties are particularly large and it is desirable to have a 'robust' design. In terms of a commercialisation strategy, the biggest risk in any programme is in the FOAK plant milestone, which can and should be de-risked, insofar as practical, by various supporting programmes (e.g. materials testing, component test facilities, etc). For instance, should the $Q = 10$ campaign in ITER be successful, in the sense that the plasma performs as expected, then we would have a much better basis of extrapolation and higher confidence in the predictive capability of high-fidelity modelling. Grounds, certainly, for reducing ΔH—for EU-DEMO at least, where the operational scenario is relatively similar to $Q = 10$ in ITER.

Nth-of-a-kind (NOAK) power plants, would be able to leverage experimental and operational data from the FOAK plant. Put simply, epistemic uncertainties surrounding the performance of plasmas in NOAK plants would be significantly lower than for a FOAK. As such, NOAK plants could be designed with lower margins for epistemic uncertainties, higher performance, and/or lower cost.

Nevertheless, as the success of any fusion commercialisation strategy effectively hinges on the success of its FOAK fusion power plant, it stands to reason that the FOAK should be developed such that its mission(s) can be accomplished even if plasma performance is lower than anticipated. This is particularly poignant for those fusion commercialisation efforts whose FOAK plant has been assigned the mission of net electricity production, but with a 'low' $P_{el,net}$, e.g. ≈50–100 MWe. Such plants tend to have high recirculating power fractions, and low $P_{el,net}/P_{fus}$; the objective usually being to produce some net electricity from fusion as cheaply as possible. Unless such a FOAK plant has been designed with adequate margins for plasma uncertainties, there is a non-negligible risk that even a slight under-performance in the plasma could result in $P_{el,net} < 0$, potentially jeopardising the commercialisation drive as whole.

7. Summary and conclusions

A novel approach for explicitly and robustly accounting for epistemic uncertainties in plasma confinement in the 0D design of tokamaks is presented, in which q_{95} is used to apply a design margin on confinement in terms of H. The approach is specifically conceived to insulate the engineering design of future tokamak fusion power plants from epistemic confinement uncertainties insofar as possible, facilitating the design process.

The PROCESS code is used to explore the EU-DEMO design space in terms of A, R_0, q_{95}, and $P_{el,net}$. We formulate a proposal for a new EU-DEMO design point at $A = 2.8$ which addresses some key shortcomings of the EU-DEMO 2017 baseline [3, 4]), in particular by the inclusion of an explicit and quantified design margin for epistemic confinement uncertainties, and a considerable reduction in divertor heat loads during re-attachment.

For the EU-DEMO assumptions made and the design space explored herein, providing a margin for epistemic confinement uncertainties of $\Delta H = 0.11$ is tantamount to a reduction of ≈150 MWe in $P_{el,net}$, compared with $\Delta H = 0$ and the same plasma geometry. A hefty price to pay, perhaps, but one that leads to a more robust design, and which enables the engineering of EU-DEMO to proceed with almost no propagation of confinement uncertainties.

Acknowledgments

We would like to thank the PROCESS code authors, and Dr E. Fable (IPP), Dr C. Luongo (EUROfusion), Dr J. Lorenzo (BSC), Dr X. Sarasola (EPFL), Prof. R. Ambrosino (CREATE), and Dr L. Giannini (EUROfusion) for many stimulating discussions and useful insights.

This work has been carried out within the framework of the EUROfusion Consortium, funded by the European Union via the Euratom Research and Training Programme (Grant Agreement No. 101052200—EUROfusion). Views and opinions expressed are however those of the author(s) only and do not necessarily reflect those of the European Union or the European Commission. Neither the European Union nor the European Commission can be held responsible for them.

Appendix A. $P_{fus} \propto I_p^c$

Calculating P_α from the reaction rate, we have:

$$P_\alpha \propto \int_V n_i^2 \overline{\sigma\nu}_{DT}(T_i)\,\mathrm{d}V \tag{A.1}$$

where $\overline{\sigma\nu}_{DT}(T_i)$ is the D-T thermonuclear reaction rate. The reaction rate depends on T_i^2 between ≈10.5–18.5 keV (see e.g. [39]), and on T_i above 18.5 keV, though this is in fact a gradual transition. In large fusion reactors with relatively peaked temperature profiles ($T_{i,core} > 23$ keV), we typically see the majority of the fusion power coming from the core region, where density is highest, despite the volume being relatively small. Therefore, in the core, we have $P_\alpha \propto n^2 T$.

Ignoring auxiliary heating and all loss terms, such that $P_\alpha = P_{net}$, we can state:

$$W_{th} = P_\alpha \tau_E(P_\alpha) \propto nT \tag{A.2}$$

re-arranging equation (A.2) for T, and taking the IPB98(y,2) scaling law (see equation (8)) for τ_E we now have:

$$P_\alpha \propto n^2 \frac{P_\alpha I_p^{0.93} n^{0.41} P_\alpha^{-0.69}}{n} \tag{A.3}$$

remembering that at constant f_{GW} we have $n \propto I_p$, and $P_{fus} \approx 5P_\alpha$, we finally have:

$$P_{fus} \propto I_p^{2.34/0.69} = I_p^{3.39}. \tag{A.4}$$

Note that this simplified approach effectively assumes ignition, and in practice it is unreasonable to ignore radiation losses in P_{net} (which also depend on n^2). The strong dependence of P_{fus} on I_p and n is also found in integrated modelling frameworks, see [76], where a more modest dependence of $I_p^{2.3—2.4}$ is seen, pointing to a potential deficiency in the scaling law.

Appendix B. TF coil stresses

A detailed description of the simplified, cylindrical (plane stress) structural model for the TF coil stresses can be found in [6], and recent improvements (not used in this work) can be found in [77]. The stress constraint is applied to the inboard midplane of the TF coil, where stress (ignoring 3D effects and peaking factors) is maximal and out-of-plane forces can reasonably be ignored.

The total TF coil current, I_{TF}, is determined by Ampère's law such that the vacuum toroidal field is B_T at R_0:

$$I_{TF} = \frac{2\pi}{\mu_0} R_0 B_T. \tag{B.1}$$

A uniform and constant current density in the winding pack, j_{TF} is assumed in the cylindrical model:

$$j_{TF} = \frac{I_{TF}}{\pi \left(r_{WP,out}^2 - r_{WP,in}^2\right)} \tag{B.2}$$

where $r_{WP,in}$ and $r_{WP,out}$ are the inner and outer radii of the inboard TF winding pack.

The field at a radius r inside the winding pack is toroidally uniform in the cylindrial model and is taken as:

$$B_T(r) = \frac{\mu_0}{2\pi r} j\pi \left(r^2 - r_{WP,in}^2\right) \tag{B.3}$$

The radial Lorentz forces per unit volume is then $F_r = j_{TF} B_T(r)$.

The radial and azimuthal stress components, σ_r and σ_θ, are calculated using a two-layer cylindrical model (nose and winding pack layers) in which the winding pack is treated as homogeneous and its stiffness is calculated as a smeared property, see [6] for a full description. The stiffness of the insulation, pure superconductor, and Helium is taken as 0. For SS316 and copper we take the Young's moduli as $E_{SS316} = 205$ GPa and $E_{Cu} = 117$ GPa. A general Poisson ratio of $\nu = 0.3$ is assumed.

The vertical stress component, σ_z, is calculated as the vertical force over area, where only the area of the structural components (nose, casing, and jacket), $A_{structural}$, is taken:

$$\sigma_z = \frac{f_{inboard} F_z}{A_{structural}} \tag{B.4}$$

where F_z is the vertical force, taken as the integral of the vertical Lorentz forces on the upper half of the TF coil, see equation (B.5), and $f_{inboard}$ is the fraction of the vertical force borne by the inboard TF leg, taken here as 0.5.

$$F_z = \frac{\mu_0}{4\pi} \frac{I_{TF}^2}{n_{TF}} \ln\left(\frac{r_{TF,outboard}}{r_{TF,inboard}}\right). \tag{B.5}$$

The structural contribution of the plasma-side casing is ignored in the two-layer model, but is included in $A_{structural}$ for the calculation of σ_z.

The stresses in the casing and jacket, $\sigma_{TF,case}$ and $\sigma_{TF,WP}$, which are constrained in the optimisation problem, are taken as Tresca stress criteria, of the form:

$$\sigma_{Tresca} = \frac{1}{2} \max\left(|\sigma_r - \sigma_\theta|, |\sigma_r - \sigma_z|, |\sigma_\theta - \sigma_z|\right). \tag{B.6}$$

The azimuthal stress is typically much greater than the radial stress, such that the last term in equation (B.6) is selected, meaning that the constraint function is usually continuous and twice-differentiable.

Appendix C. CS coil fatigue constraint

For this study, a semi-elliptical ($\kappa_{crack} = 3$) planar surface crack of 1 mm^2 cross-sectional area is assumed in the CS CICC jacket. SS316-LN Paris fatigue material properties are taken as $C = 3.86\times10^{-11}$ m/cycle, $m = 0.386$, and $K_{IC} = 150\,\text{MPa}\sqrt{m}$, from [78]. The crack-growth Paris law model is generally considered to be conservative, and work on an alternative probabilistic approach to fatigue assessment is ongoing elsewhere. As such, we have taken safety factors of 1.0 for the number of cycles, the fracture toughness, and the crack size.

The C and m constants depend on the mean stress ratio, r_σ:

$$r_\sigma = \frac{\sigma_{min}}{\sigma_{max}} = \frac{\sigma_{res}}{\sigma_{hoop} + \sigma_{res}} \tag{C.1}$$

where σ_{res} is the residual manufacturing hoop stress in the CS jacket, taken as 150 MPa. σ_{hoop} is the peak hoop stress occurring in the CS jacket due to normal operation.

The C constant is then corrected to account for the mean stress ratio, as suggested by Walker [79]:

$$C_r = C(1 - r_\sigma)^{m(m_W - 1)} \tag{C.2}$$

where m_W is the Walker coefficient, for which we take a typical value in fatigue studies; $m_W = 0.5$.

δK is a function of the crack geometry and σ_{hoop}, calculated using a reduced model based on finite element studies of stresses in cracks [80].

Following [67], a lifecycle approach is used to integrate the Paris law with a simple Euler method to determine the number of cycles that the CS can withstand. For a given crack with vertical and radial dimensions a and c, with a fixed size increment δ_{crack}:

$$\begin{aligned} dn_{cycles,CS_{j+1}} &= \frac{\delta_{crack}}{C_r \delta K_{max}^m} \\ \delta K_{max} &= \max\left(\delta K_a\left(a_j, c_j\right), \delta K_c\left(a_j, c_j\right)\right) \\ da_{j+1} &= \delta_{crack}\left(\frac{\delta K_a}{\delta K_{max}}\right)^m \\ dc_{j+1} &= \delta_{crack}\left(\frac{\delta K_c}{\delta K_{max}}\right)^m \end{aligned} \tag{C.3}$$

giving $n_{cycles,CS}$. The integration is terminated when the crack dimensions exceed the thickness or length of the CS CICC jacket, or $K_{max} \geqslant K_{IC}$.

The required number of cycles, n_{cycles}, to reach L_{dpa} is then:

$$n_{cycles} = \frac{L_{fpy}}{8760\tau_{pulse}} \tag{C.4}$$

where L_{fpy} is given in equation (27).

Note the dependence on τ_{pulse} in this constraint is not adjusted for in terms of $(\tau_{pulse})^*$. Should the multiple assumptions made in the context of this constraint function all hold true, and the $(\cdot)^*$ case come to pass, we would have $(L_{dpa})^* \approx 64$ dpa $< L_{dpa}$.

Appendix D. Pulse length calculation

PROCESS calculates the poloidal flux balance over a reactor pulse using a crude equilibrium in which the plasma vertical field (calculated using an expression from [54], see equation (D.1)) is balanced by the outer PF coils (PF3 and PF4, by ITER naming convention). All PF coils are used to cancel out the varying field from the CS along the plasma midplane during a pulse

$$B_V = -\frac{\mu_0}{4\pi}\frac{I_p}{R_0}\left(\ln\left(8A\right) + \beta_{p,thermal} + \frac{l_i}{2} - 1.5\right). \tag{D.1}$$

The PF coils positions are crudely parameterised as follows:

$$\begin{aligned} r_{PF1} = r_{PF6} &= R_0 - f_{r,PF1,6}\delta a \\ z_{PF1} &= z_{TF,up} + dz_{PF1,6} \\ z_{PF6} &= -z_{TF,up} - dz_{divertor} - dz_{PF1,6} \\ r_{PF2} = r_{PF5} &= \sqrt{\left(r_{TF,outboard} + dr_{PF2..5}\right)^2 - z_{PF2}^2} \\ z_{PF2} = -z_{PF5} &= f_{z,PF2,5}a \\ r_{PF3} = r_{PF4} &= \sqrt{\left(r_{TF,outboard} + dr_{PF2..5}\right)^2 - z_{PF3}^2} \\ z_{PF3} = -z_{PF4} &= f_{z,PF3,4}a \end{aligned} \tag{D.2}$$

with $f_{r,PF1,6} = -1.825$, $dz_{PF1,6} = 0.86$ m, $dr_{PF2..5} = 1.5$ m, $f_{z,PF2,5} = 2.8$, and $f_{z,PF3,4} = 1.0$, with the TF coil maximum outer radius, $r_{TF,outboard}$, the maximum upper vertical extent of the TF coil, $z_{TF,up}$, and the divertor height $dz_{divertor}$.

The CS coil is centred at the midplane, with its height calculated as:

$$h_{CS} = 2f_{z,CS}z_{TF,up} \tag{D.3}$$

where $f_{z,CS} = 0.9$ is the ratio of the CS height to the TF height.

The PF currents are solved for by least-squares minimisation of an $\mathbf{Ax} - \mathbf{b}$ problem using singular value decomposition, in which $\mathbf{A}$ is a response matrix of elliptical integrals for each PF coil to each position on the plasma midplane in terms of B_r and B_z.

The flux swing contribution from the PF coils is then calculated from the resulting currents at start and end of flat-top with elliptical integrals for the poloidal flux.

The flux available from the solenoid is calculated as:

$$\Phi_{CS} = \frac{\pi}{3}B_{CS,max}\left(R_{CS,i}^2 + R_{CS,i}R_{CS,o} + R_{CS,o}^2\right). \tag{D.4}$$

The resistive flux consumption is calculated as:

$$\Phi_{res} = C_{Ejima}\mu_0 R_0 I_p \tag{D.5}$$

where C_{Ejima} is the Ejima coefficient [81], taken here as 0.2, and not 0.3 as in previous EU-DEMO studies [3, 9] based on some preliminary detailed ramp-up studies using a flight simulator [82]. The resulting lower resistive consumption is due to the higher temperature (which is reached relatively quickly during ramp-up) and lower resistivity of the plasma in EU-DEMO.

The inductive flux consumption is calculated as:

$$\Phi_{ind} = \mu_0 R_0\left(\frac{l_i}{2} + l_e\right)I_p \tag{D.6}$$

where l_i is calculated as per equation (24), l_e is the normalised plasma external inductance calculated as a function of A and κ using a fit found in [83].

The flux available for flat-top operation is then:

$$\Phi_{flattop} = \Phi_{CS} + \Phi_{PF} - \Phi_{res} - \Phi_{ind}. \tag{D.7}$$

Finally, the pulse length is calculated as:

$$\tau_{pulse} = \frac{\Phi_{flattop}}{v_{loop}}. \tag{D.8}$$

This procedure differs in a number of ways from more sophisticated ones in which a series of constrained optimisation problems are solved on 2D axisymmetric equilibria, see e.g. [84]. In particular, there are some known discrepancies in terms of l_i and some of the assumptions made regarding the PF coil contributions to the flux swing. The calculation for l_i is known to produce values much higher than are expected in EU-DEMO ($\approx$1.15 vs. $\approx$0.8). Yet the only place l_i is used is when calculating the poloidal flux balance and the pulse length, and the present formulation was found to result in far better estimates of the flux available for the flat-top when compared with typical equilibrium calculations carried out by the CREATE team [84] at different aspect ratios.

Despite these discrepancies, reasonable agreement on $\Phi_{flattop}$ between PROCESS and detailed PF system design studies has been found in the past.

Appendix E. $P_{el,net}$: WCLL vs. HCPB

When the EU-DEMO 2017 baseline was generated, WCLL and HCPB blankets performed similarly in terms of overall plant efficiency in PROCESS: the higher thermal to electric conversion efficiency of the HCPB blanket was largely offset by the higher electrical power required for the He compressors, such that it was approximately equivalent to the WCLL blanket in terms of $P_{el,net}$. Since then, both blankets have been designed and studied in more depth, and HCPB blankets now perform significantly better than WCLL blankets in terms of net electrical power, see e.g. [14].

Table E.8 shows the different blanket assumptions for WCLL and HCPB in G1 and the most recent values, and the resulting $P_{el,net}$ as calculated for the $A = 2.8$ design point presented in this work. Note that the EU-DEMO G1 design point, with HCPB G1 assumptions, resulted in $P_{el,net} = 500$ MWe. With WCLL 2024 assumptions, the EU-DEMO G1 design point would result in $P_{el,net} = 465$ MWe.

Table E.8. WCLL and HCPB input assumptions for G1 and in 2024, and resulting $P_{el,net}$ for the $A = 2.8$, $R_0 = 8.6$ m design point.

Parameter	WCLL G1	HCPB G1	WCLL 2024	HCPB 2024
$\eta_{thermal}$	0.310	0.375	0.316	0.375
e_{mult}	1.269	1.269	1.200	1.350
$P_{BB,in}$ (MPa)	—	8.0	—	8.0
dP_{BB} (MPa)	—	0.550	—	0.268
$T_{BB,in}$ (K)	—	573	—	573
dT_{BB} (K)	—	200	—	220
η_{isen}	—	0.90	—	0.85
η_{elec}	0.87	0.87	0.90	0.90
f_{pump}	0.0050	—	0.0111	—
$P_{el,net}$ (MWe)	371	378	350	485

In the case of HCPB blankets, f_{pump} is calculated based on the pressure and temperature drop and assuming an ideal gas, with $\gamma_{He} = 1.667$:

$$\begin{aligned} f_{pressure} &= \left(\frac{P_{BB,in}}{P_{BB,in} - dP_{BB}}\right)^{\frac{\gamma_{He}-1}{\gamma_{He}}} \\ T_{in,compressor} &= \frac{T_{BB,in}}{f_{pressure}} \\ f_{pump} &= \frac{T_{in,compressor}}{\eta_{isen} dT_{BB}} \left(f_{pressure} - 1\right) \end{aligned} \tag{E.1}$$

with the electrical pumping power then being calculated as per equation (29). The work done to the coolant by pumps is added to the total thermal power of the blanket.

ORCID iDs

C. Bourdelle https://orcid.org/0000-0002-4096-8978
M. Siccinio https://orcid.org/0009-0006-7870-6769
A. Spagnuolo https://orcid.org/0000-0001-8416-3349
S. Wiesen https://orcid.org/0000-0002-3696-5475

References

[1] ITER Physics Expert Group on Confinement and Transport, ITER Physics Expert Group on Confinement Modelling and Database and ITER Physics Basis Editors 1999 Chapter 2: Plasma confinement and transport *Nucl. Fusion* **39** 2175
[2] Lux H., Kemp R., Fable E. and Wenninger R. 2016 Radiation and confinement in 0D fusion systems codes *Plasma Phys. Control. Fusion* **58** 075001
[3] Wenninger R. and Kembleton R. 2017 DEMO1 reference design—2017 March "EU DEMO1 2017" *Technical Report* EFDA_D_2NDSKT (EUROfusion)
[4] Siccinio M., Graves J., Kembleton R., Lux H., Maviglia F., Morris A., Morris J. and Zohm H. 2022 Development of the plasma scenario for EU-DEMO: status and plans *Fusion Eng. Des.* **176** 113047
[5] Kovari M., Kemp R., Lux H., Knight P., Morris J. and Ward D. 2014 "PROCESS": a systems code for fusion power plants—part 1: physics *Fusion Eng. Des.* **89** 3054–69
[6] Kovari M., Fox F., Harrington C., Kembleton R., Knight P., Lux H. and Morris J. 2016 "PROCESS": a systems code for fusion power plants—part 2: engineering *Fusion Eng. Des.* **104** 9–20
[7] Federici G., Baylard C., Beaumont A. and Holden J. 2021 The plan forward for EU DEMO *Fusion Eng. Des.* **173** 112960
[8] Federici G. *et al* 2016 Overview of the design approach and prioritization of R&D activities towards an EU DEMO *Fusion Eng. Des.* **109–111** 1464–74
[9] Morris J. and Kembleton R. 2018 Physics and magnet baseline February 2018 *Technical Report* EFDA_D_2MGYZP (EUROfusion)
[10] Zohm H., Träuble F., Biel W., Fable E., Kemp R., Lux H., Siccinio M. and Wenninger R. 2017 A stepladder approach to a tokamak fusion power plant *Nucl. Fusion* **57** 086002
[11] Tran M.Q. 2020 WPHCD design issue statement 2NRPX5 *Technical Report* (EUROfusion)
[12] Hernandez F.G. 2020 Internal deliverable BB-1.2.1-T007-D001: design and integration studies 2020 *Technical Report* EFDA_D_2NUZCR (EUROfusion)
[13] Arena P. *et al* 2023 Design and integration of the EU-DEMO water-cooled lead lithium breeding blanket *Energies* **16** 2069
[14] Barucca L. *et al* 2021 Pre-conceptual design of EU DEMO balance of plant systems: objectives and challenges *Fusion Eng. Des.* **169** 112504
[15] Federici G. *et al* 2019 Overview of the DEMO design-staged approach in Europe *Nucl. Fusion* **59** 066013
[16] Federici G., Holden J., Baylard C. and Beaumont A. 2021 The EU DEMO staged design approach in the pre-concept design phase *Fusion Eng. Des.* **173** 112959
[17] Lux H., Siccinio M., Biel W., Federici G., Kembleton R., Morris A., Patelli E. and Zohm H. 2019 Implications of uncertainties on European DEMO design *Nucl. Fusion* **59** 066012
[18] Miralles-Dolz E., Pearce A., Morris J. and Patelli E. 2022 Toward DEMO power plant concept selection under epistemic uncertainty *IEEE Trans. Plasma Sci.* **50** 4440–5

[19] Romanelli M. *et al* (EFDA-JET Contributors) 2014 JINTRAC: a system of codes for integrated simulation of tokamak scenarios *Plasma Fusion Res.* **9** 3403023

[20] Pereverzev G.V. and Yushmanov P. 2002 ASTRA - Automated system for transport analysis in tokamaks IPP 5/98 Max-Planck-Institut für Plasmaphysik (IPP) (available at: https://pure.mpg.de/rest/items/item_2138238_1/component/file_2138237/content)

[21] Bourdelle C., Garbet X., Imbeaux F., Casati A., Dubuit N., Guirlet R. and Parisot T. 2007 A new gyrokinetic quasilinear transport model applied to particle transport in tokamak plasmas *Phys. Plasmas* **14** 112501

[22] Bourdelle C., Citrin J., Baiocchi B., Casati A., Cottier P., Garbet X. and Imbeaux F. (JET Contributors) 2015 Core turbulent transport in tokamak plasmas: bridging theory and experiment with QuaLiKiz *Plasma Phys. Control. Fusion* **58** 014036

[23] Staebler G.M., Kinsey J.E. and Waltz R.E. 2007 A theory-based transport model with comprehensive physics[a)] *Phys. Plasmas* **14** 055909

[24] Staebler G.M. and Kinsey J.E. 2010 Electron collisions in the trapped gyro-Landau fluid transport model *Phys. Plasmas* **17** 122309

[25] Citrin J. and Mantica P. 2023 Overview of tokamak turbulence stabilization by fast ions *Plasma Phys. Control. Fusion* **65** 033001

[26] Siccinio M. *et al* 2023 Development of a plasma scenario for the EU DEMO tokamak reactor *29th IAEA Fusion Energy Conference (FEC 2023)* (*London, United Kingdom, 16–21 October 2023*) IAEA-CN-316-1661 (available at: https://conferences.iaea.org/event/316/contributions/28003/)

[27] Kinsey J.E., Staebler G.M. and Waltz R.E. 2008 The first transport code simulations using the trapped gyro-Landau-fluid model[a)] *Phys. Plasmas* **15** 055908

[28] Staebler G.M., Candy J., Howard N.T. and Holland C. 2016 The role of zonal flows in the saturation of multi-scale gyrokinetic turbulence *Phys. Plasmas* **23** 062518

[29] Staebler G.M., Candy J., Belli E.A., Kinsey J.E., Bonanomi N. and Patel B. 2020 Geometry dependence of the fluctuation intensity in gyrokinetic turbulence *Plasma Phys. Control. Fusion* **63** 015013

[30] Staebler G., Belli E.A., Candy J., Kinsey J., Dudding H. and Patel B. 2021 Verification of a quasi-linear model for gyrokinetic turbulent transport *Nucl. Fusion* **61** 116007

[31] Bourdelle C. 2025 Integrated modelling of tokamak plasmas: progresses and challenges towards ITER operation and reactor design (in preparation)

[32] Snyder P., Groebner R., Hughes J., Osborne T., Beurskens M., Leonard A., Wilson H. and Xu X. 2011 A first-principles predictive model of the pedestal height and width: development, testing and ITER optimization with the EPED model *Nucl. Fusion* **51** 103016

[33] Snyder P.B., Osborne T.H., Burrell K.H., Groebner R.J., Leonard A.W., Nazikian R., Orlov D.M., Schmitz O., Wade M.R. and Wilson H.R. 2012 The EPED pedestal model and edge localized mode-suppressed regimes: studies of quiescent H-mode and development of a model for edge localized mode suppression via resonant magnetic perturbations[a)] *Phys. Plasmas* **19** 056115

[34] Saarelma S. 2016 Predictive pedestal modelling for DEMO *Technical Report* (EUROfusion) (available at: https://idm.euro-fusion.org/default.aspx?uid = 2MSZ4T)

[35] Burckhart A. *et al* (the ASDEX Upgrade Team) 2023 Experimental evidence of magnetic flux pumping in ASDEX Upgrade *Nucl. Fusion* **63** 126056

[36] Bosch H.-S. and Hale G.M. 1992 Improved formulas for fusion cross-sections and thermal reactivities *Nucl. Fusion* **32** 611–31

[37] Martin Y.R. and Takizuka T. (andthe ITPA CDBM H-mode Threshold Database Working Group) 2008 Power requirement for accessing the H-mode in ITER *J. Phys.: Conf. Ser.* **123** 012033

[38] Summers H.P. 2004 The ADAS user manual, version 2.6 (available at: www.adas.ac.uk)

[39] Jean J. 2011 HELIOS: a zero-dimensional tool for next step and reactor studies *Fusion Sci. Technol.* **59** 308–49

[40] Fidone I., Giruzzi G. and Granata G. 2001 Synchrotron radiation loss in tokamaks of arbitrary geometry *Nucl. Fusion* **41** 1755–7

[41] Albajar F., Johner J. and Granata G. 2001 Improved calculation of synchrotron radiation losses in realistic tokamak plasmas *Nucl. Fusion* **41** 665–78

[42] International Atomic Energy Agency 1990 ITER physics design guidelines: 1989 *Technical Report* INIS-mf–12641 (International Atomic Energy Agency (IAEA) (available at: http://inis.iaea.org/search/search.aspx?orig_q = RN:21068960)

[43] Uckan N.A., International Atomic Energy Agency Vienna (Austria) and ITER Physics Group 1990 *ITER physics design guidelines: 1989*

[44] Wenninger R. *et al* 2016 The physics and technology basis entering European system code studies for DEMO *Nucl. Fusion* **57** 016011

[45] Bachmann C. *et al* 2024 Re-design of EU DEMO with a low aspect ratio *Fusion Eng. Des.* **204** 114518

[46] Coleman M. 2021 An integrated design framework for future nuclear fusion power reactors *PhD Thesis* Apollo - University of Cambridge Repository (https://doi.org/10.17863/CAM.77387)

[47] Albanese R., Ambrosino R. and Mattei M. 2014 Summary of the main results on the DEMO vertical stability calculation as part of the aspect ratio study *Technical Report* EFDA_D_2L4NM (EUROfusion)

[48] Hofmann F. *et al* 2002 Extension of the TCV operating space towards higher elongation and higher normalized current *Nucl. Fusion* **42** 743

[49] Wenninger R. *et al* 2015 Advances in the physics basis for the European DEMO design *Nucl. Fusion* **55** 063003

[50] Gribov Y., Kavin A., Lukash V., Khayrutdinov R., Huijsmans G., Loarte A., Snipes J. and Zabeo L. 2015 Plasma vertical stabilisation in ITER *Nucl. Fusion* **55** 073021

[51] Humphreys D. *et al* 2009 Experimental vertical stability studies for ITER performance and design guidance *Nucl. Fusion* **49** 115003

[52] Sauter O., Angioni C. and Lin-Liu Y.R. 1999 Neoclassical conductivity and bootstrap current formulas for general axisymmetric equilibria and arbitrary collisionality regime *Phys. Plasmas* **6** 2834–9

[53] Sauter O., Angioni C. and Lin-Liu Y.R. 2002 Erratum: "Neoclassical conductivity and bootstrap current formulas for general axisymmetric equilibria and arbitrary collisionality regime" [Phys. Plasmas 6, 2834 (1999)] *Phys. Plasmas* **9** 5140

[54] Wesson J. 2004 *Tokamaks* 3rd edn (Oxford University Press)

[55] Corato V. *et al* 2016 Common operating values for DEMO magnets design for 2016 *Technical Report* (EUROfusion)

[56] Park J.H. and Pereslavtsev P. 2024 Main nuclear responses of the DEMO tokamak with different in-vessel component configurations *Appl. Sci.* **14** 936

[57] Flammini D., Villari R., Moro F., Pizzuto A. and Bachmann C. 2016 Neutronics studies for the design of the European DEMO vacuum vessel *Fusion Eng. Des.* **109–111** 784–8

[58] Fischer U., Bachmann C., Jaboulay J.-C., Moro F., Palermo I., Pereslavtsev P. and Villari R. 2016 Neutronic performance issues of the breeding blanket options for the European

DEMO fusion power plant *Fusion Eng. Des.* **109–111** 1458–63
[59] Noce S., Moro F., Romanelli F. and Villari R. 2019 Nuclear analysis of the single module segment WCLL DEMO *Fusion Eng. Des.* **147** 111207
[60] Federici G., Biel W., Gilbert M., Kemp R., Taylor N. and Wenninger R. 2017 European DEMO design strategy and consequences for materials *Nucl. Fusion* **57** 092002
[61] Narcisi V., Ciurluini C., Padula G. and Giannetti F. 2022 Analysis of EU-DEMO WCLL power conversion system in two relevant balance of plant configurations: direct coupling with auxiliary boiler and indirect coupling *Sustainability* **14** 5779
[62] Siccinio M., Federici G., Kembleton R., Lux H., Maviglia F. and Morris J. 2019 figure of merit for divertor protection in the preliminary design of the EU-DEMO reactor *Nucl. Fusion* **59** 106026
[63] Uckan N.A., Tolliver J.S., Houlberg W.A. and Attenberger S.E. 1988 Influence of fast alpha diffusion and thermal alpha buildup on tokamak reactor performance *Fusion Technol.* **13** 411–22
[64] Bottura L. and Bordini B. 2009 $J_C(B,T,\varepsilon)$ parameterization for the ITER Nb_3Sn production *IEEE Trans. Appl. Supercond.* **19** 1521–4
[65] Morris J., Kemp R., Kovari M., Last J. and Knight P. 2015 Implications of toroidal field coil stress limits on power plant design using process *Fusion Eng. Des.* **98–99** 1118–21
[66] Bachmann C. 2016 Estimate of the main EM loads in DEMO depending on the aspect ratio *Technical Report* EFDA_D_2MBSE3 (EUROfusion)
[67] Lorenzo J., Sarasola X. and Mantsinen M. 2020 Fatigue stress assessment in fusion magnet components *Technical Report* EFDA_D_2PBDRG (EUROfusion)
[68] Sarasola X., Bruzzone P., Sedlak K., Corato V., Giannini L., Bachmann C., Luongo C. and Siccinio M. 2023 Parametric studies of the EU DEMO central solenoid *IEEE Trans. Appl. Supercond.* **33** 1–5
[69] Paris P. and Erdogan F. 1963 A critical analysis of crack propagation laws *J. Basic Eng.* **85** 528–33
[70] Hamada K., Nakajima H., Kawano K., Takano K., Tsutsumi F., Okuno K., Suzuki T. and Fujitsuna N. 2007 Optimization of JK2LB chemical composition for iter central solenoid conduit material *Cryogenics* **47** 174–82
[71] Campbell D.J. *et al* (Domestic Agencies and ITER Collaborators) 2019 Innovations in technology and science R&D for ITER *J. Fusion Energy* **38** 11–71
[72] Morris J. *et al* 2024 PROCESS (available at: https://github.com/ukaea/PROCESS)
[73] Powell M.J.D. 1978 A fast algorithm for nonlinearly constrained optimization calculations (available at: https://api.semanticscholar.org/CorpusID:115696750)
[74] Wolff D., Coleman M., Cooper D., Crofts O., Horne J., Keep J. and Loving A. 2017 The impact on remote maintenance of varying the aspect ratio and number of TF coils for DEMO *Fusion Eng. Des.* **124** 553–7
[75] Langeslag S., Sgobba S., Libeyre P., Marcinek D. and Zhang Z. 2015 Extensive characterisation of advanced manufacturing solutions for the ITER central solenoid pre-compression system *Fusion Eng. Des.* **98–99** 2015–9
[76] Palermo F., Fable E., Angioni C., Siccinio M. and Zohm H. 2019 Scaling laws from theory-based modeling for different regimes in the DEMO fusion reactor *Nucl. Fusion* **59** 096010
[77] Swanson C.P.S. *et al* 2022 Validation and results of an approximate model for the stress of a Tokamak toroidal field coil at the inboard midplane (arXiv:2206.14699)
[78] ITER Organization 2009 ITER design description document, TF coils and structures *Technical Report* ITER_D_2MVZNX (ITER)
[79] Walker K. 1970 The effect of stress ratio during crack propagation and fatigue for 2024-T3 and 7075-T6 aluminum *Effects of Environment and Complex Load History on Fatigue Life* (ASTM International) (https://doi.org/10.1520/STP32032S)
[80] Newman J. and Raju I. 1983 Stress-intensity factor equations for cracks in three-dimensional finite bodies *Fracture Mechanics: 14th Symposium—Volume I: Theory and Analysis* (ASTM International) pp 238–65 (https://doi.org/10.1520/STP37074S)
[81] Ejima S., Callis R., Luxon J., Stambaugh R., Taylor T. and Wesley J. 1982 Volt-second analysis and consumption in doublet III plasmas *Nucl. Fusion* **22** 1313
[82] Siccinio M. 2021 EU-DEMO pulse length sprint 2PK5UR *Technical Report* (EUROfusion)
[83] Hirshman S.P. and Neilson G.H. 1986 External inductance of an axisymmetric plasma *Phys. Fluids* **29** 790–3
[84] Albanese R., Ambrosino R., Castaldo A. and Loschiavo V. 2018 Optimization of the PF coil system in axisymmetric fusion devices *Fusion Eng. Des.* **133** 163–72